Submesoscale Eddies in the Upper Ocean of the Kuroshio Extension from High-Resolution Simulation: Energy Budget

HAIJIN CAO, a BAYLOR FOX-KEMPER, b AND ZHIYOU JINGC

^a Key Laboratory of Marine Hazards Forecasting, Ministry of Natural Resources and College of Oceanography, Hohai University, Nanjing, China

^b Department of Earth, Environmental, and Planetary Sciences, Brown University, Providence, Rhode Island ^c State Key Laboratory of Tropical Oceanography, South China Sea Institute of Oceanology, Chinese Academy of Sciences, Guangzhou, China

(Manuscript received 29 October 2020, in final form 11 April 2021)

ABSTRACT: The submesoscale energy budget is complex and remains understood only in region-by-region analyses. Based on a series of nested numerical simulations, this study investigated the submesoscale energy budget and flux in the upper ocean of the Kuroshio Extension, including some innovations for examining submesoscale energy budgets in general. The highest-resolution simulation on a ~500-m grid resolves a variety of submesoscale instabilities allowing an energetic analysis in the submesoscale range. The frequency-wavenumber spectra of vertical vorticity variance (i.e., enstrophy) and horizontal divergence variance were used to identify the scales of submesoscale flows as distinct from those of inertiagravity waves but dominating horizontal divergence variance. Next, the energy transfers between the background scales and the submesoscale were examined. The submesoscale kinetic and potential energy (SMKE and SMPE) were mainly contained in the mixed layer and energized through both barotropic (shear production) and baroclinic (buoyancy production) routes. Averaged over the upper 50 m of ROMS2, the baroclinic transfers amounted to approximately 75% of the sources for the SMKE $(3.42 \times 10^{-9} \,\mathrm{W \, kg^{-1}})$ versus the remaining 25% $(1.12 \times 10^{-9} \,\mathrm{W \, kg^{-1}})$ via barotropic downscale KE transfers. The KE field was greatly strengthened by energy sources through the boundary—this flux is larger than the mesoscale-tosubmesoscale transfers in this region. Spectral energy production, importantly, reveals upscale KE transfers at larger submesoscales and downscale KE transfers at smaller submesoscales (i.e., a transition from inverse to forward KE cascade). This study seeks to extend our understanding of the energy cycle to the submesoscale and highlight the forward KE cascade induced by upper-ocean submesoscale activities in the research domain.

KEYWORDS: Eddies; Small scale processes; Energy budget/balance; Regional models

1. Introduction

Submesoscale activities are ubiquitous in high-resolution satellite images and have received intense study via simulations and observations in recent decades. Oceanic energy cascade research beforehand tended to emphasize the large scale of climatological forcing, the mesoscale with its dominant reservoir of kinetic energy and predominant inverse cascade (Ferrari and Wunsch 2009), and the forward cascade of internal waves and microstructure turbulence. Recent studies have highlighted the role of submesoscale processes and their instabilities, as a dynamic conduit for energy transfer between large-scale and dissipation scale (e.g., Capet et al. 2008b; Thomas et al. 2013; Zhang et al. 2016; Wang et al. 2018) and as a mechanism for vertical transport of heat, salt, and biogeochemical tracers (e.g., Mahadevan and Tandon 2006; Lévy et al. 2001, 2012; Rosso et al. 2014). However, challenges associated with studying submesoscales remain (McWilliams 2016), as in situ observations of quickly evolving, intermittent events over scales of O(1-10) km are rarely clear from cruise surveys or moorings, although drifters, autonomous platforms, and new remote sensing are improving submesoscale observation techniques (e.g., Villas Boas et al. 2019; du Plessis et al. 2019; D'Asaro et al. 2020; Gentemann et al. 2020; Zhang et al. 2021).

Corresponding author: Zhiyou Jing, jingzhiyou@scsio.ac.cn

In realistic numerical simulations, the horizontal grid resolution has been too coarse to capture submesoscale flows adequately until recently (Dong et al. 2020a).

Identifying the dynamical routes for removal of large-scale energy is a challenge. Quasigeostrophic and 2D turbulence roughly following a $k^{-5/3}$ power law are characterized by an inverse energy cascade at large scales and a forward potential enstrophy cascade with minimal forward kinetic energy transfer (k^{-3} power law) in the homogenous, isotropic turbulence limit (e.g., Kraichnan 1967; Charney 1971; Cronin and Watts 1996; Tulloch et al. 2011; Kang and Curchitser 2015; Yang and Liang 2016; Pearson and Fox-Kemper 2018). In mesoscale-permitting models, the primary sinks of kinetic energy are bottom drag and vertical mixing, although cascade processes as represented through parameterizations may play a role (Pearson et al. 2017).

Thus, submesoscale processes are expected to be a mechanism for the downscale energy transfer (Ferrari and Wunsch 2009), either by barotropic kinetic energy transfers or by baroclinic mechanisms linking to potential energy transfers (Capet et al. 2008a; Fox-Kemper et al. 2008). For example, surface-trapped modes (Klein et al. 2008) can easily drive submesoscale flows with Rossby and Richardson numbers of O(1) (Thomas et al. 2008) by a variety of submesoscale instabilities such as mixed layer instability (Boccaletti et al. 2007; Fox-Kemper et al. 2008), symmetric instability that draws energy from geostrophic shear production (Hoskins 1974; Thomas et al. 2013;

Bachman et al. 2017a), lateral shear instability and barotropic conversion (Munk et al. 2000; Fox-Kemper et al. 2008; Molemaker et al. 2010; Gula et al. 2014), and centrifugal instability (Jiao and Dewar 2015). In some regions and simulations, submesoscales may even energize the mesoscale (Callies et al. 2016; Schubert et al. 2020). These instabilities form from and influence the flow shear, frontal strength, and mixed layer depth. The OSMOSIS mooring observations in the eastern North Atlantic indicate that submesoscale eddies are mainly generated through baroclinic instability with energy from buoyancy production (Buckingham et al. 2017), whereas Wang et al. (2018) showed that submesoscale eddies in the tropical Pacific Ocean on a scale of 300 km are generated through barotropic instability of the geostrophic shear. In situ observations (e.g., Callies et al. 2015; Buckingham et al. 2016; Thompson et al. 2016; Jing et al. 2016; D'Asaro et al. 2020) and high-resolution numerical simulations (e.g., Capet et al. 2008a; Klein et al. 2008; Sasaki et al. 2014; Rocha et al. 2016; Bachman et al. 2017b; Schubert et al. 2020) all suggest that submesoscales in the ocean form a continuum of chaotic nonlinear processes (Shcherbina et al. 2013), exhibiting regional uniqueness that is difficult to disentangle.

To manage the variety of submesoscale instabilities, an energy flow analysis was used to separate the barotropic and baroclinic energy routes in regions such as the Kuroshio Extension. The energetic Kuroshio Extension jet flows eastward from the coast of Japan maintaining a meandering pattern with the highest energy level of mesoscale eddies in the northwest Pacific Ocean (Tai and White 1990; Qiu et al. 1991; Qiu 2000; Nakamura and Kazmin 2003) and exchanges momentum and water masses in the Kuroshio Extension region (Waterman et al. 2011). The Kuroshio Extension system in this simulation appears to be convoluted and unstable (not shown), with variable meridional change and active eddies in this region (Qiu and Chen 2005). For the unstable phase, the geostrophic eddies shedding from the Kuroshio Extension with typical length scales close to the deformation radius tend to be highly nonlinear and unstable (Klocker et al. 2016). This situation is favorable for generating submesoscales through both baroclinic and barotropic routes (Sasaki et al. 2014; Qiu et al. 2014). A series of nested numerical simulations used here (ranging from ROMS0 at \sim 7.5-km resolution to ROMS2 at \sim 0.5 km) permit most geostrophic-branch barotropic and baroclinic submesoscale instabilities in the Kuroshio Extension region during the late spring (fully described in section 2a; Jing et al. 2021; Dong et al. 2020a). These high-resolution simulations were used to study the spectral energy budget and transfer routes near the strong persistent front.

This modeling study has four main goals:

- Defining the submesoscale range in frequency-wavenumber space, as inspired by examining the spectra of vorticity and divergence which reveals the submesoscale as a region of elevated divergence.
- Clarifying the barotropic and baroclinic energy transfer routes by presenting the energy cycle emphasizing flows into the submesoscale range.
- 3) Identifying the dominant energy routes energizing submesoscales in the Kuroshio Extension region.

 Quantifying the scale-dependent kinetic and potential energy fluxes with spectral energy budgets.

The remainder of this paper is organized as follows. Section 2 describes the model setup, validates the model skill with satellite and in situ observations, and frames the analysis method. Section 3 identifies, separates, and quantifies the submesoscale kinetic energy (SMKE) and potential energy (SMPE), exploiting the frequency—wavenumber spectra of kinetic energy, potential energy, vertical vorticity variance (i.e., enstrophy), and horizontal divergence variance. Section 4 presents a detailed energy budget analysis of the upper-ocean submesoscales and also investigates the wavenumber spectra of the components making up the barotropic and baroclinic energy fluxes and their sensitivity to horizontal resolution. Finally, section 5 summarizes the conclusions of this study.

2. Model description and analysis method

a. High-resolution simulation

In this study, the Regional Oceanic Modeling System (ROMS) is used to conduct a series of one-way-nested simulations of the Kuroshio Extension (Shchepetkin and McWilliams 2005). The parent model (ROMS0) with a coarse horizontal resolution of \sim 7.5 km covers the northwest Pacific Ocean (Fig. 1a) and a 20-yr spinup was performed to reach a statistically equilibrated state before starting the one-way nesting simulations on child grids of \sim 1.5 km (ROMS1) and \sim 0.5 km (ROMS2). For brevity, the simulations are also referred to as low-, middle-, and highresolution simulations. These simulations were run on a curvilinear, latitude-longitude grid and terrain-following S-coordinates of 60 vertical levels, with refined vertical level thicknesses in the mixed layer ranging from 0.3 to 5.0 m. The subgrid vertical mixing of momentum and tracers is based on the K-profile parameterization (KPP) scheme (Large et al. 1994). The lateral mixing is parameterized as a linear combination of Laplacian and biharmonic mixing, scaled with the grid size (Lemarié et al. 2012). A biased third-order upstream scheme for the tracer and momentum advection provides numerical lateral diffusivity and viscosity, respectively, in the lateral direction (Shchepetkin and McWilliams 2009). These ROMS configurations have been successfully applied in the regional submesoscale simulations, e.g., the Gulf Stream, the Atlantic Ocean, and the eddy-active northwest Pacific Ocean (Capet et al. 2008b; Gula et al. 2014; Capuano et al. 2018; Jing et al. 2021). In these simulations, surface atmospheric forcing including wind stress, heat, and freshwater fluxes, were derived from the daily mean climatology of the Quick Scatterometer (QuikSCAT) dataset and the International Comprehensive Ocean Atmosphere Dataset (ICOADS) (Woodruff et al. 2011). The boundary and initial information for the largest domain were taken from the monthly averaged Simple Ocean Data Assimilation (SODA) ocean climatology outputs (Carton and Giese 2008). The modeling results (e.g., regional circulation, mixed layer depth, and energy level of mesoscale eddies) have been compared against satellite measurements and available historical in situ observations. Comparisons to measurements on multiple platforms show that the simulations are sufficiently

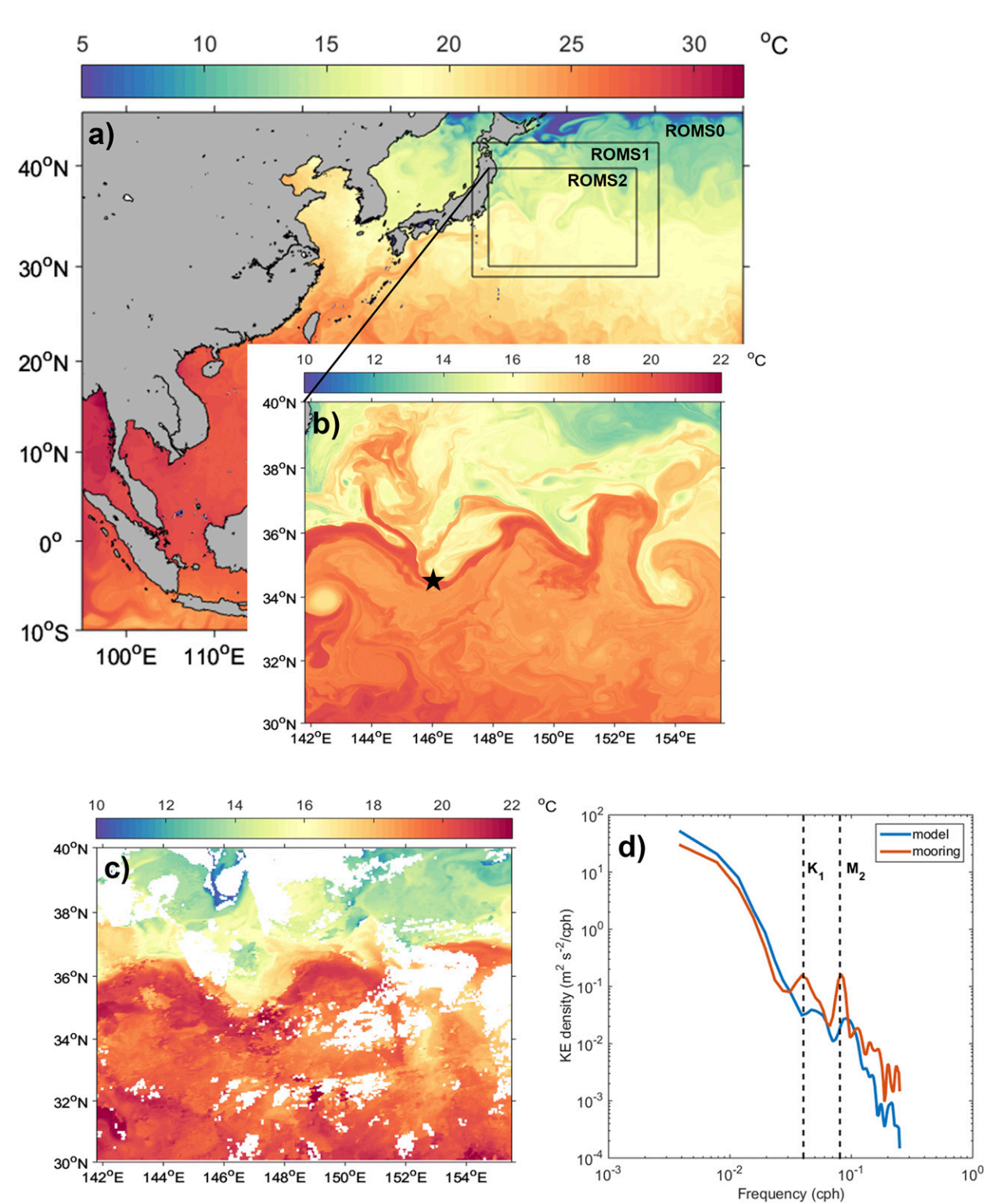


FIG. 1. (a) Model surface temperature in domains of nested models at horizontal resolutions of \sim 7.5 km (ROMS0), \sim 1.5 km (ROMS1), and \sim 0.5 km (ROMS2), respectively. (b) The simulated sea surface temperature compared with (c) that from MODIS *Aqua* on 1 May 2018. (d) The comparison of the upper-ocean (50–200 m) velocity spectra between the model and the KESS mooring at 34.5°N, 146.0°E [black star in (b)].

accurate to characterize the climatological conditions of the northwest Pacific upper ocean.

The ROMS0 was run for another two years after the spinup to provide daily boundary information for ROMS1 (\sim 1.5 km), and the ROMS1 tends to reach a numerically equilibrated state in about a month. The ROMS1 was run for one year and provided daily boundary information for the nested simulation of ROMS2. The ROMS2 was run for 6 weeks (the first 4 weeks are for spinup), and the outputs in the last two weeks from 28 April to 12 May were used for the diagnostic analysis of this study (capturing a quasi-stationary period for the meandering flow of the Kuroshio Extension). Therefore, the energy level of submesoscales remained steady without seasonal variation during this period. A comparison of the simulations shows that they did not drift too much (Cao and Jing 2020, manuscript submitted to J. Geophys. Res. Oceans). The highest-resolution simulation (ROMS2) can resolve a wide range of submesoscale instabilities and was used for the energetic analysis of submesoscale eddies. As shown in the following sections, the 2-hourly output from ROMS2 can clearly depict the evolution of larger submesoscale motions, although smaller submesoscale instabilities are likely affected by resolution (Bachman and Taylor 2014). Despite the parameterization for subgrid processes, the ROMS2 simulation with a horizontal scale of ~500 m is sufficient to figure out the energy route at submesoscales.

The research domain is shown in Fig. 1a. Figures 1b and 1c compare the ROMS2 surface temperature to the MODIS Aqua data from https://oceancolor.gsfc.nasa.gov/ in the same month (1 May 2018). The simulated temperature field roughly agrees with the satellite observation. In addition, the location of the flow stream and the scale of the meander in the simulation are close to those in the satellite image. The in situ velocity data observed by the mooring of the Kuroshio Extension System Study (KESS) project (available at https://uskess.whoi.edu/overview/dataproducts/) were used to validate the kinetic energy (KE) level of the simulation (Fig. 1d). The KE spectra of the mooring observation and the simulation are comparable in both amplitude and spectral slope, although the tidal frequencies were underestimated because of the absence of tidal forcing in the simulation.

b. Energetic diagram

Energetics analysis quantifies the energy budget: the energy sources, sinks, and exchanges among different energy reservoirs. To examine the energy exchange between submesoscale and larger and/or slower scales (called the "background" to denote that it can contain small and slow or large and fast scales), the following energy equations were derived from the hydrostatic, Boussinesq equations for seawater:

$$\frac{\partial u}{\partial t} + \mathbf{u} \cdot \nabla u - f v = -\frac{1}{\rho_0} \frac{\partial p}{\partial x} + F_u + D_u, \tag{1}$$

$$\frac{\partial \boldsymbol{v}}{\partial t} + \mathbf{u} \cdot \nabla \boldsymbol{v} + \boldsymbol{f}\boldsymbol{u} = -\frac{1}{\rho_0} \frac{\partial \boldsymbol{p}}{\partial \boldsymbol{y}} + \boldsymbol{F_v} + \boldsymbol{D_v}, \tag{2}$$

$$\frac{\partial p}{\partial z} = -\rho g,\tag{3}$$

$$\frac{\partial \rho}{\partial t} + \mathbf{u} \cdot \nabla \rho = F_{\rho} + D_{\rho}, \tag{4}$$

$$\nabla \cdot \mathbf{u} = 0, \tag{5}$$

where $\mathbf{u} = (u, v, w)$ is the velocity vector, f is the Coriolis frequency, ρ is the density, $\rho_0 = 1025\,\mathrm{kg\,m^{-3}}$ is the reference density, and p denotes the pressure. The last two terms in Eqs. (1), (2), and (4), F and D, represent the forcing and dissipation, respectively, which include viscosity, diffusivity, and subgrid parameterizations. The density equation, Eq. (4), is a combination of the salinity and temperature equations according to the equation of state. A Reynolds decomposition for 3D flow is employed to separate the background flow and submesoscale perturbations as

$$\mathbf{u} = \overline{\mathbf{u}} + \mathbf{u}'. \tag{6}$$

The eddy state has been commonly derived from the time-mean or spatial filtering of the velocity field in previous studies of energetics (Cronin and Watts 1996; Aiki and Richards 2008; Grooms et al. 2013). In this study, the perturbation velocity was derived by both high-pass filtering in time and spatial domains, with a sharp spectral cutoff in the Fourier transform spectrum to make an approximate Reynolds average. The specific scale and frequency partition is marked in the frequency—wavenumber spectrum in Fig. 4 below. Then, the residual flow was considered as the background flow [indicated by the overbar in Eq. (6)], which contains large, slow variability, but also large, fast variability and small, slow variability.

The length scale of submesoscale instabilities in the mixed layer can be estimated by (Boccaletti et al. 2007)

$$L = \frac{NH_m}{f} \sqrt{1 + \frac{1}{Ri}},\tag{7}$$

where H_m is the depth of the mixed layer and N is the vertical buoyancy frequency. Here the mean N over the mixed layer is used. Also, the linear instability time scale can be estimated by (Callies et al. 2015)

$$T = \frac{N}{f\sqrt{\left(\frac{\partial \overline{u}}{\partial z}\right)^2 + \left(\frac{\partial \overline{v}}{\partial z}\right)^2}},\tag{8}$$

In submesoscale turbulence, cascades alter the energy-containing length scale and the eddy turnover time significantly away from these linear instability values (Fox-Kemper et al. 2008; Bachman and Fox-Kemper 2013). Thus, a different method for identifying the nonlinear cascade range of scales constituting the submesoscales is needed.

As previously mentioned, the subgrid processes and 3D turbulence are parameterized, so the submesoscales are expected to represent the smallest resolved scales in ROMS2. With these guidelines in mind, high-pass filtering with steep spectral cutoff in both time and space was conducted to obtain the high-wavenumber, high-frequency perturbation [primed in Eq. (6)] velocities that are defined as submesoscale flows, not based on linear instability scales but on energy-containing scales. The filtering was tested to be robust. The common

emphasis for submesoscales is their intense vorticity (Capet et al. 2008a; Thomas et al. 2008) and divergence (D'Asaro et al. 2018; Pearson et al. 2019, 2020), which will serve as the basis for targeting their range of scales. In our analysis, the submesoscale is defined as a horizontal scale of less than 20 km and also a time scale of less than 1.5 days. A detailed analysis of choosing these particular bounds for the definition of the submesoscale follows in section 3.

After the Reynolds averages are defined, the KE budget by submesoscale perturbations can be obtained by multiplying momentum Eqs. (1) and (2) by u' and v', respectively, and taking the Reynolds average of their sum gives

$$\frac{\partial}{\partial t}(SMKE) = \underbrace{-\frac{1}{2}\nabla \cdot \left[\mathbf{u}(\mathbf{u}'^{2} + v'^{2})\right]}_{ADK} \underbrace{-\frac{1}{\rho_{0}}\nabla \cdot \left(\mathbf{u}'p'\right)}_{PW} \underbrace{-\frac{1}{\rho_{0}}g\overline{\rho'w'}}_{PKE} \underbrace{-\frac{1}{\rho_{0}}g\overline{\rho'$$

where SMKE refers to the hydrostatic submesoscale kinetic energy, $(u'^2 + v'^2)/2$. The cross energy terms are negligible (e.g., $\overline{\mathbf{u}' \cdot \overline{\mathbf{u}}} \approx 0$), because the average is assumed to be a Reynolds average. The first and second terms on the right side represent the advection of and pressure work on SMKE [advection of submesoscale kinetic energy (ADK) and pressure work (PW)], respectively. The third term represents the buoyancy production, which is the energy conversion from SMPE to SMKE, which is typical of baroclinic instability pathways (hereafter referred to as PKE). The fourth term denotes the shear production, i.e., energy transfer from large-scale KE to SMKE through submesoscale rearrangement of momentum that changes the large-scale shear, also known as the barotropic instability pathway (background-to-submesoscale KE transfer, hereafter referred to as BSK). Note that both horizontal and vertical shear production are counted in BSK. The terms D_{K2} and F_{K2} are the diffusion and forcing of SMKE, which are calculated as the residual of the other terms in the energy budget equation.

Similarly, the potential energy (PE) budget by the submesoscale perturbations can be expressed as

$$\frac{\partial}{\partial t}(\text{SMPE}) = \underbrace{-\nabla \cdot \left[\mathbf{u} \left(\frac{g^2 \rho'^2}{2\rho_0^2 N^2}\right)\right]}_{\text{ADP}} \underbrace{-\frac{g^2}{\rho_0^2 N^2} \overline{\rho' \mathbf{u}' \cdot \nabla \rho} + \frac{1}{\rho_0} g}_{\text{BSP}} \underbrace{\frac{\overline{\rho' w'}}{\rho' \overline{w'}}}_{-PKE} + \underbrace{\overline{D_{P2}} + \overline{F_{P2}}}_{D+F}, \tag{10}$$

where a linear definition for the available potential energy (APE) is used (Gill 1982; Kang and Fringer 2010) as follows,

APE =
$$\frac{g^2(\rho - \rho_r)^2}{2\rho_0^2 N^2}$$
, (11)

where ρ_r is the reference density. Based on these definitions, the SMPE can be expressed as

SMPE =
$$\frac{g^2 \rho'^2}{2\rho_0^2 N^2}$$
. (12)

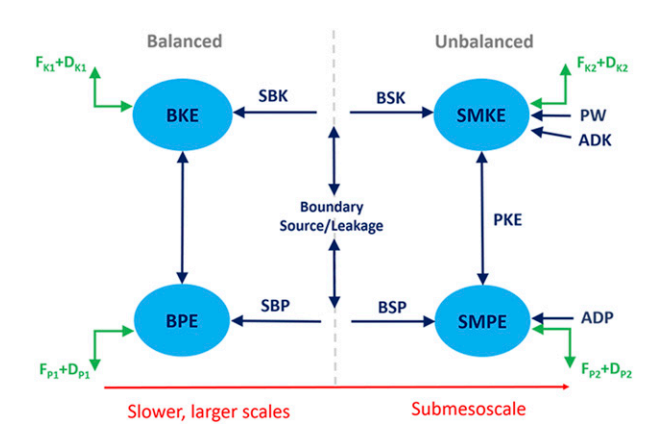


FIG. 2. Diagram of Lorenz (1955) energy cycle as evaluated between background scales (all nonsubmesoscales) and submesoscales (scales smaller than 20 km and faster than 1.5 days). Four energy reservoirs are defined as background kinetic energy (BKE), background potential energy (BPE), submesoscale kinetic energy (SMKE), and submesoscale potential energy (SMPE). BSK is the KE transfer from the background scales and submesoscale. Likewise, BSP is the PE transfer from the background and submesoscale. PKE represents the energy release of submesoscale available potential energy via buoyancy production, indicating baroclinic instability pathways. PW, ADK, and ADP represent the pressure work and advection effects on kinetic and potential energy, respectively. Note that additional boundary terms of energy leakage/source representing the energy from (to) outer domains are required for the energetic analysis in regional seas. The sum of SBK and BSK (SBP and BSK) is expected to be zero when there is no boundary leakage/source for KE (PE). The green arrows denote the combined effects of atmosphere forcing $(F_K \text{ and } F_P)$ and dissipation $(D_K \text{ and } D_P)$.

The SMPE budget equation results from using a locally linear state equation to arrive at a tracer equation for density in the same form as Eq. (4), i.e., neglecting nonlinear thermosteric effects such as cabbelling. Note that a completely satisfactory definition of APE corresponding to the Lorenz (1955) approach does not exist for seawater (Huang 1999), but this approach is negligibly different from other more computationally expensive ones (Saenz et al. 2015), especially at the ocean surface where the submesoscales are highly active, compressibility effects are small, and this energy budget is evaluated. These definitions were selected for ease of comparison with approaches taken in other basins (Kang and Fringer 2010; Kang and Curchitser 2015). In this study, these budgets were calculated only over the upper 50 m surface region of ROMS2 over the whole zonal and meridional region. The terms on the right-hand side of Eq. (10) represent the advection (ADP), buoyancy production energy conversion from SMPE to SMKE (again typical of PKE), submesoscale horizontal buoyancy production (BSP), and diffusion and forcing that are determined by the residual. So the term associated with the vertical shear of horizontal velocity is bounded by the residual in the PE budget. The two energy equations provide an estimate of the submesoscale energy production terms. An energy budget diagram (Fig. 2) is employed to chart the energy conversion between the submesoscale and background scales.

The large and slow scales, including the mesoscales, are the primary reservoir and constitute the background potential and kinetic energy, referred to as BPE and BKE, respectively. In Fig. 2, BSK and BSP represent the KE and PE transfer from background scales to the submesoscale (Kang and Curchitser 2015; Yan et al. 2019). BSK and BSP have also been widely interpreted as barotropic (shear production) and baroclinic (buoyancy production) energy conversions to smaller scales (e.g., Cronin and Watts 1996; Kang and Curchitser 2015). The green arrows denote the combined effects of atmospheric forcing and dissipation, which are estimated by the residual of the other terms.

The energy budget of the background scales is formed by finding the Reynolds average momentum equation and forming a mean energy equation from its dot product with $\overline{\mathbf{u}}$. Collecting the key terms from the energy budget formed from the Reynolds averaged Eqs. (1)–(5), we obtain

$$SBK = -\overline{[\overline{u}\nabla \cdot (\mathbf{u}'u') + \overline{v}\nabla \cdot (\mathbf{u}'v')]} = BndyKE-BSK, \quad (13)$$

$$SBP = -\frac{g^2}{\rho_0^2 N^2} \overline{\rho} \nabla \cdot \overline{\mathbf{u}' \rho'} = BndyPE-BSP.$$
 (14)

SBK and SBP are also known as the background kinetic and potential energy change due to eddy momentum fluxes (i.e., Reynolds stresses) and density fluxes (Chen et al. 2014). It seems ambiguous to interpret that which term (BSK or SBK) represents the energy conversion from one form to another (Holopainen 1978).

Calculus identities guarantee that the term formed by the dot product with the Reynolds stress is equal and opposite to the shear production in a closed basin, when the global integrals of the boundary terms (BndyKE, BndyPE) are guaranteed to be zero (Chen et al. 2014). However, for a fractional basin ocean domain, these boundary terms can and do provide additional sources and sinks for the energy budget. In an open domain, the sum of SBK and BSK (or SBP and BSP) tends to be nonzero but instead equals a boundary term contributing to the KE (PE) field. Care is needed, and there is a choice to which reservoir BndyKE and BndyPE are applied. Here we chose to interpret BndyKE as a source to the BKE, which results in the BSK transfer energizing the SMKE (and SBK playing a less important role). Similarly, we chose to interpret BndyPE as energizing the BPE, which then makes BSP the path to energizing the SMPE. See the appendix for a more detailed derivation and discussion. Alternative approaches to diagnosis of the energy budget focusing on high-energy Lagrangian flow features (Jamet et al. 2020) may help to address some of these uncertainties in localized budgets and help explain the tendency in Lagrangian observations to vary systematically from Eulerian observations in the fluxes of KE across scales (Pearson et al. 2019, 2020). The physical interpretations of the boundary terms are further discussed in the following sections where the energy terms are evaluated.

3. Submesoscale kinetic and potential energy

a. Energy levels of BKE, SMKE, and SMPE

This section estimates the energy levels of BKE (background KE), SMKE (submesoscale KE), and SMPE (submesoscale PE).

BPE (background PE) cannot be estimated without an arbitrary definition of reference level. Figure 3 shows the energy levels of BKE, SMKE, and SMPE averaged over the upper 50 m of the research domain from the ROMS2 simulation. It shows that the submesoscale energy (SMKE + SMPE) is orders of magnitude smaller than the BKE and that SMKE + SMPE tends to be stronger where the BKE is large, as the energetic background flow is favorable for generating submesoscales. As shown in Fig. 3d, the KE spectrum has a slope of -2.4 from mesoscale to submesoscale in the mixed layer and the slope drops to -3 (geostrophic prediction) below the mixed layer. The flattening of the mixed layer KE spectrum is thought to arise from the submesoscale motions, especially fronts (Capet et al. 2008a). Note that the spectra are transformed from 2D spectra with the assumption of isotropy, which could be partly violated due to spatial heterogeneity [see appendix A in Cao et al. (2019) for details]. In addition, to reduce the Gibbs phenomena, we created periodic boundaries by mirroring the research domain in both x and y directions to obtain robust spectra. The time-mean wavenumber spectra in the Fig. 3d were tested for robustness by comparison to other windowing choices. However, the spectral roll-off starting from ~5 km is not consistent with observations, thus, the spectra below 5 km (about 10 times the grid size) presumably result from a numerical issue leading to the excessive damping of KE at scales smaller than 5 km. Fortunately, the submesoscales in this region reach up to 20 km for about a half-decade of reliable submesoscale dynamics. In the depth-averaged horizontal plane (Fig. 3e), the jet region (between 33° and 37°N) has more energetic BKE, SMKE, and SMPE, among which the BKE is approximately two orders of magnitude larger than the SMKE or SMPE. As seen from the horizontally averaged vertical profile (Fig. 3f), the SMKE and SMPE underwent a dramatic decrease from 1.17×10^{-3} and $0.90 \times 10^{-3} \,\mathrm{J\,kg^{-1}}$ at the surface to 0.50×10^{-3} and $0.31 \times$ 10^{-3} J kg⁻¹ at the base of the mixed layer, respectively, indicating that the submesoscale energy is higher in the mixed layer. The average mixed layer depth marked by the red dashed line is defined to be the shallowest depth where the density difference is 0.03 kg m⁻³ from the surface layer (de Boyer Montégut et al. 2004), and the energy budget will be taken over the upper 50 m, including the entire mixed layer and some of the pycnocline.

b. Spectral estimates of the submesoscale range

A further look into the kinetic and potential energy can be achieved by the spectra as functions of frequency and wavenumber defined by

KE =
$$\frac{1}{2}\hat{\mathbf{u}}^* \cdot \hat{\mathbf{u}}$$
, PE = $\frac{1}{2}\hat{b}^* \frac{\hat{b}}{N^2}$, (15)

where $b = -g(\rho/\rho_0)$ is the buoyancy and $\widehat{()}$ denotes the Fourier transform. The frequency-wavenumber (F-K) spectrum can be derived from the model data using these definitions. The details of deriving the spectrum can be found in Cao et al. (2019). In Fig. 4, both the kinetic and potential energy continuously decrease (ROMS2 simulation at $z = -5 \,\mathrm{m}$) from larger, slower to smaller, quicker scales along the wavenumber or frequency axis. The submesoscale range used in this study is also marked by the gray-line rectangle boxes, and the blue double arrows denote the energy exchange between different

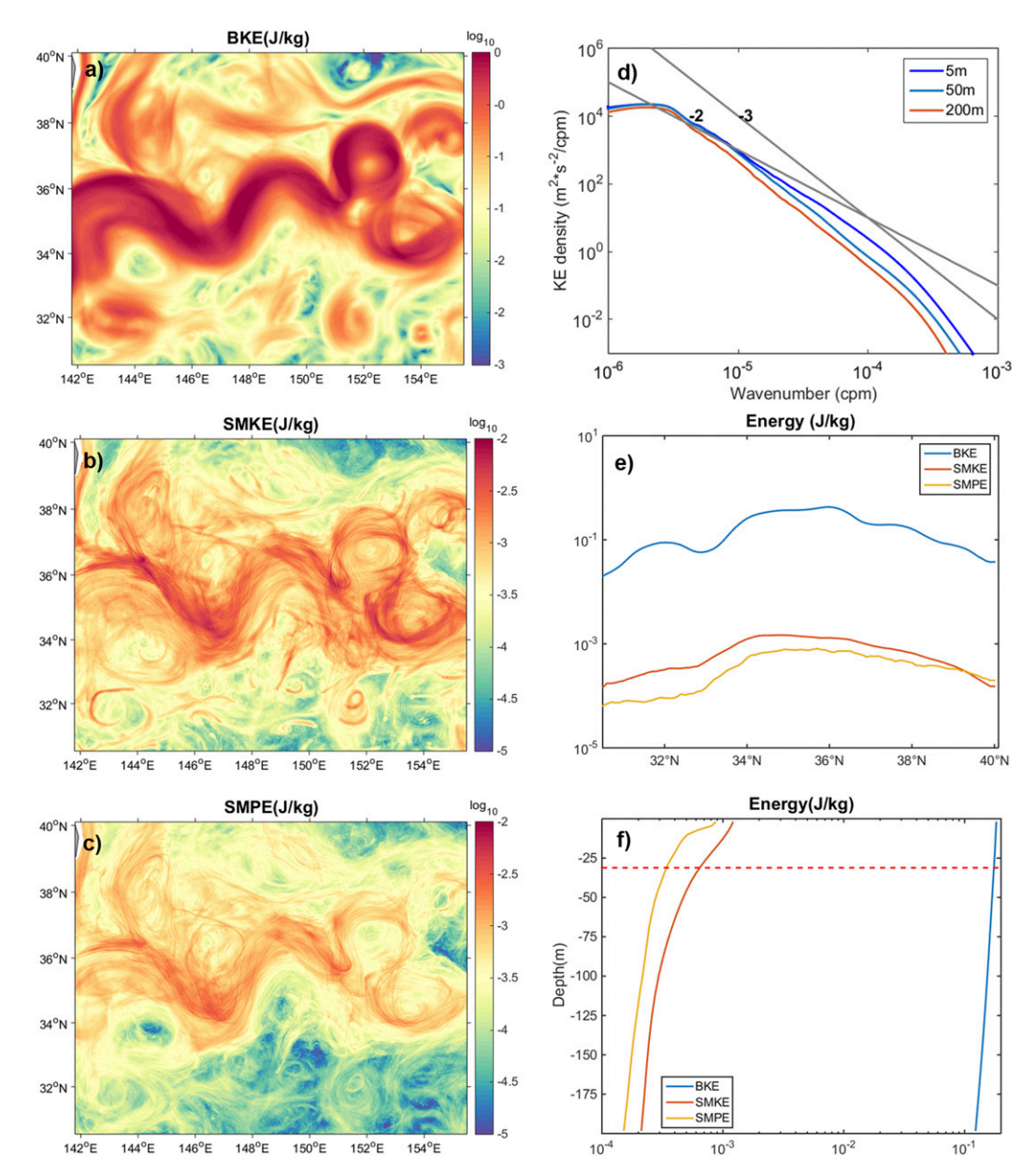


FIG. 3. Maps of averaged energy level of (a) BKE, (b) SMKE, and (c) SMPE. (d) The wavenumber spectrum of KE. The -2 and -3 power line are plotted for reference. (e) The zonally averaged BKE, SMKE, and SMPE. (f) The vertical profile of the three energy terms. The red dashed line denotes the averaged mixed layer depth.

spaces. In Fig. 4, no clear submesoscale energy peak is recognizable in either of the spectra, as SMKE or SMPE is orders of magnitude smaller than the mesoscale energy. This is consistent with the 1D wavenumber spectrum and energy content figures (Fig. 3). Instead, the vertical vorticity ($\zeta = v_x - u_y$) variance (or enstrophy) and horizontal divergence (Div = $u_x + v_y$) variance spectra (formed from the Fourier transforms of vorticity and divergence just as the energy spectra are formed from velocity and buoyancy) more clearly isolate the submesoscales as those with high density of vorticity and divergence variability.

The submesoscales have pronounced rotational and divergent effects at submesoscales (e.g., Pearson et al. 2017; Torres et al. 2018; Cao et al. 2019), which are reflected in the enstrophy and divergence variance F–K spectra. As shown in Fig. 5a, the normalized enstrophy F–K spectrum at the near-surface layer $(z=-5\,\mathrm{m})$ displays two remarkable peaks, reflecting the F–K regions of the mesoscale and submesoscale eddies, respectively, due to their high vorticity concentrations. Furthermore, the submesoscale enstrophy spectrum peak coincides with the divergence variance spectrum peak (Figs. 5a,b), suggesting the quasigeostrophically unbalanced convergence of submesoscale

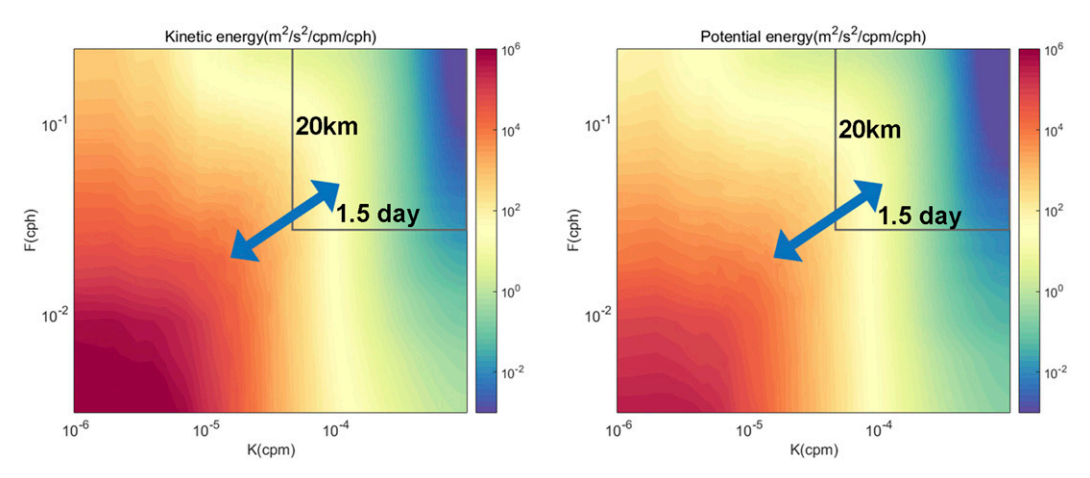


FIG. 4. Frequency–wavenumber spectra of kinetic and potential energy at z = -5 m. The submesoscale is marked by the gray-line rectangle boxes, and the double arrows denote the energy transfer between different scales.

motions. Dynamically, submesoscales differ from mesoscales as characterized by an enhancement of horizontal divergence associated with their higher Rossby number allowing them to have stronger ageostrophic transport (D'Asaro et al. 2018).

Notably, the enstrophy and divergence variance spectra rationalize our selected scale partition to isolate the submesoscales. The horizontal divergence reaches its maximum at wavelengths of $\sim\!8$ km, which is wrapped in the defined submesoscale

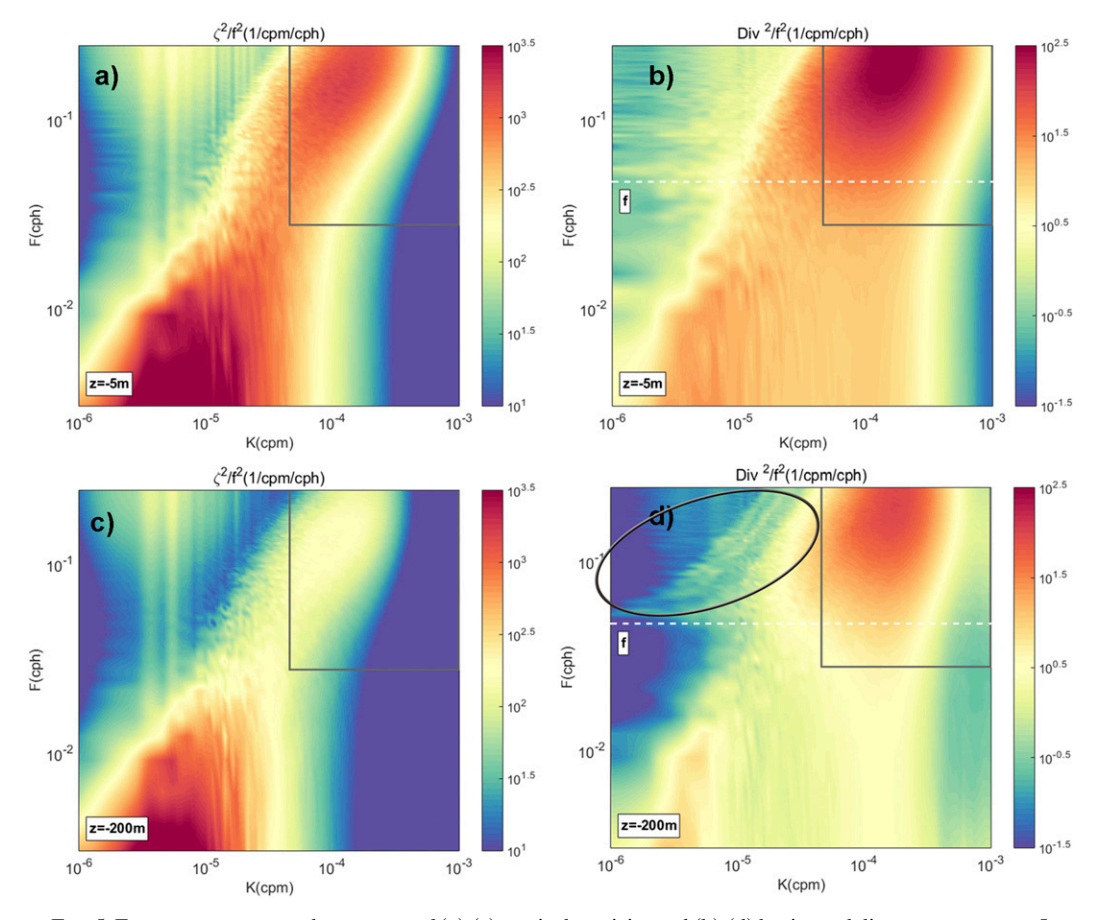


FIG. 5. Frequency—wavenumber spectra of (a),(c) vertical vorticity and (b),(d) horizontal divergence at z=-5 m and z=-200 m, respectively. The submesoscale is marked by the gray-line rectangle boxes, and the inertial gravity wave band is marked by the ellipse. The white dashed lines in (b) and (d) indicate the inertial frequency.

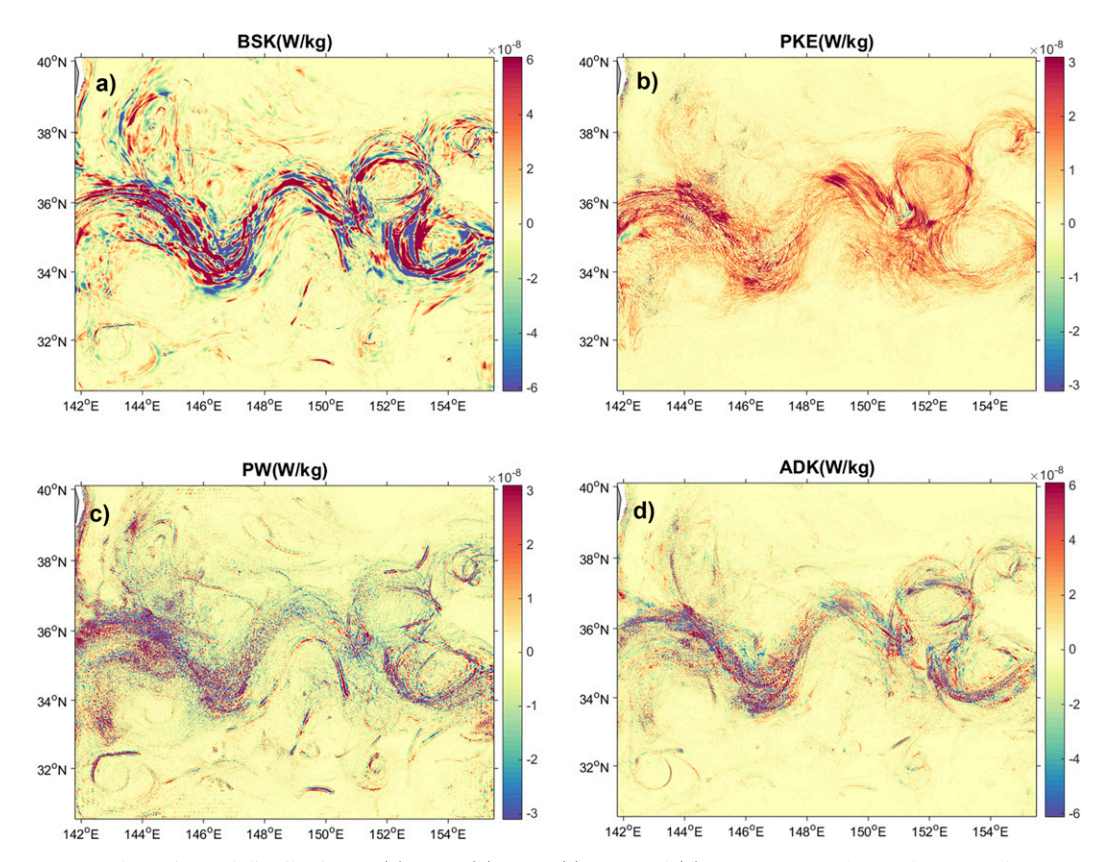


FIG. 6. Horizontal distribution of (a) BSK, (b) PKE, (c) PW, and (d) ADK averaged over the upper 50 m.

range (<20 km) in this study. Compared to the near-surface spectra within the mixed layer, the submesoscale vorticity at 200-m depth is dramatically reduced, while the mesoscale vorticity remains high, indicative of energetic mesoscale eddy effects near 100 km (a comparison between Figs. 5a,c). A typical requirement for the development of submesoscale instabilities is the low stratification in the mixed layer (Boccaletti et al. 2007; Fox-Kemper et al. 2008; Thomas et al. 2008), where the energetic submesoscale divergence arises from the submesoscale fronts and instabilities and through turbulent cascades develops broadband power-law-like spectra. While in the deeper layers, inertia-gravity waves become important for the horizontal divergence (Torres et al. 2018) and appear as energized wave banded regions of the F-K spectrum where the free, linear inertia-gravity wave dispersion relations lie. The divergence variance spectrum below the mixed layer (Fig. 5d) shows a weak but distinct banded divergence signal in the high-frequency, low-wavenumber space (highlighted by an ellipse): the signature of inertia-gravity waves. Within the mixed layer (Fig. 5b), the gravity wave signal is not apparent. Note that inertia-gravity wave motions are expected to be underestimated because of the absence of highfrequency wind stresses and tidal forcing in the simulation. As in Figs. 5c and 5d, there appears to be some submesoscale variance at the 200-m layer which is well below the mixed layer. The mechanisms for the ageostrophic motions are investigated in detail by Cao and Jing (2020, manuscript submitted to

J. Geophys. Res. Oceans) and are identified as ageostrphic frontal effects. Herein, we focus on the energy budget primarily within the mixed layer.

4. Energy budget analysis and discussion

a. Submesoscale kinetic energy budget

The high-resolution model output allows an estimate of each form of SMKE production [background-to-submesoscale KE transfer (BSK), advection of KE (ADK), buoyancy production (PKE), and pressure work (PW), respectively]. In Fig. 6, these energy production terms delineate the submesoscale eddy variability with positive/negative values denoting the submesoscale energy generation/sink. They are more active along the jet than at the flanks. This is because the jet enhances the flow shear and forms a large-scale front with great horizontal buoyancy gradient, which is favorable for the generation of submesoscales via baroclinic instability and frontogenesis.

In Fig. 6a, the BSK—a combination of the effects of Reynolds stress, horizontal and vertical shear, and the BndyKE influence of outer domains—is intensified near the jet with a positive-negative pattern that can be interpreted as the injection (positive values) and loss (negative values) of SMKE. The eddy-mean interaction is complicated because various processes underlie bidirectional energy transfers (i.e., forward energy transfer is driven by submesoscale instabilities; while the flow strain could

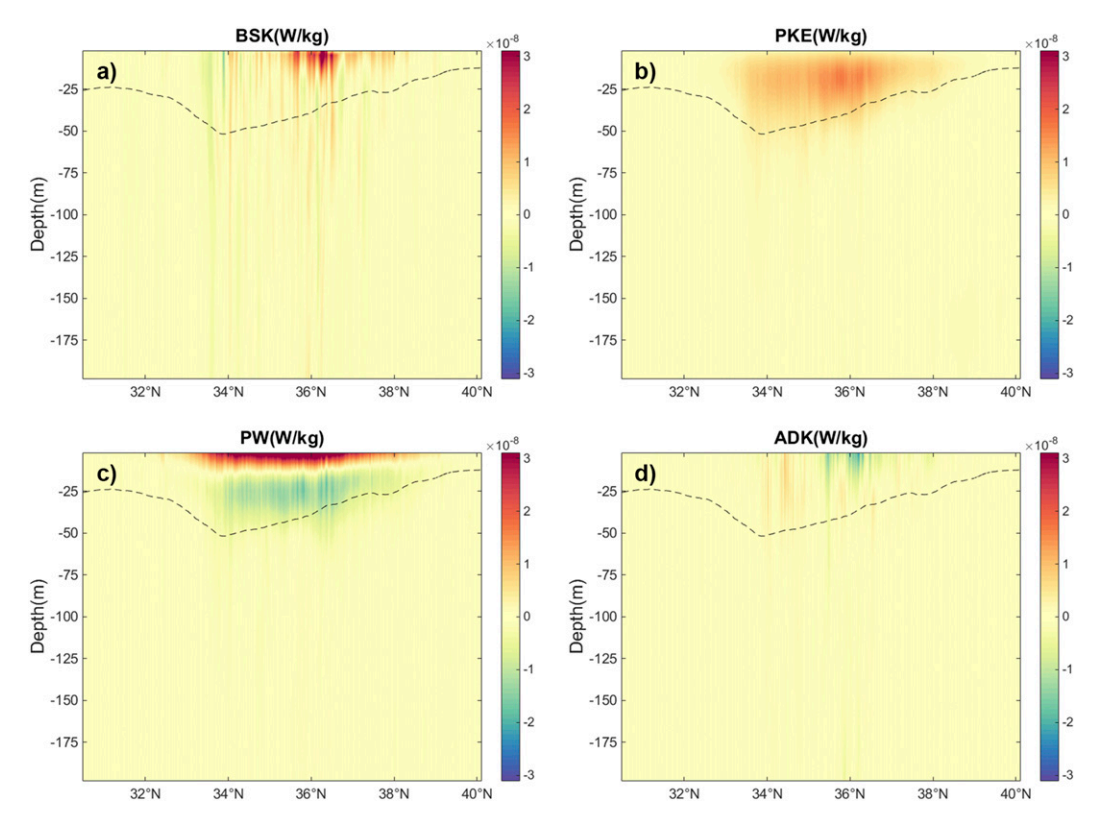


FIG. 7. Zonal-mean latitude–depth sections of (a) BSK, (b) PKE, (c) PW, and (d) ADK. The black dashed lines denote the zonally averaged mixed layer depth.

stabilize the horizontal shear instability and cause an energy transfer from submesoscale kinetic energy to the background kinetic energy (negative BSK: Gula et al. 2014; Brannigan et al. 2017), or high-frequency eddies can interact to drive lowerfrequency motions (Arbic et al. 2014). In contrast, the submesoscale PKE (potential-to-kinetic energy transfer)—known to generate SMKE from baroclinic instability modes—is mostly positive in the research domain, indicative of a continuous energy transfer from SMPE to SMKE associated with processes such as mixed layer instability (Fox-Kemper et al. 2008) and frontogenesis (e.g., Capet et al. 2008b; Suzuki et al. 2016). PW is positive in the upper layers, acting to energize the submesoscale flows; conversely, the negative PW in the lower layers partially balances the PKE, acting to stabilize the base of the mixed layer. The SMKE is reduced by PW during mixed layer restratification, which tends to restore geostrophy (Cao and Jing 2020, manuscript submitted to J. Geophys. Res. Oceans). In the zonally averaged plots (Fig. 7), the BSK is highly intensified in the surface boundary layers at the jet, but the PKE can energize the whole mixed layer and reaches its maximum in the middle of the mixed layer as in parameterization theory (Fox-Kemper et al. 2008). The mean mixed layer depth is marked by dashed lines in the figures. PKE and BSK are the largest and second largest producers of SMKE, respectively. The net contribution of pressure work and advection (PW and ADK) is minor (submesoscale advection is not important in our research domain), which is fortunate due to uncertainties

in the interpretation of energy sources these terms can induce (Plumb 1983). The BndyKE source is large, but in the chosen framing where it is applied to the BKE, only BSK needs to be analyzed in the SMKE budget.

In the zonal-mean, latitude-vertical section plot (Fig. 8a), the ADK presents a modest positive impact in the south but a negative impact in the north, indicating opposing effects on the two flanks of the jet. It is unclear why this pattern exists—it may be a coincidence of the location of the eddies incompletely canceling (Fig. 6). In the vertical profile (Fig. 8b), submesoscale energy production occurs mainly in the mixed layer for most terms. Among them, the PW yields a significant energy input in the surface boundary layer of 0–15 m but remarkable negative work at depths of 20–50 m, indicating vertical transfer of submesoscale energy. The negative work tends to reduce the submesoscale kinetic energy at the base of the mixed layer and opposes the PKE there (Fig. 8b), although the vertically integrated contribution of pressure in the mixed layer is not of great importance.

b. Submesoscale potential energy budget

Figures 9-11 show the horizontal and vertical distributions of BSP and ADP production, respectively, as in the SMPE equation. Removal of SMPE by PKE is not shown because it is already shown as a production of SMKE in the previous section and Figs. 6-8. The BSP averaged over the upper 50 m (Fig. 9a) was mostly positive in the research domain

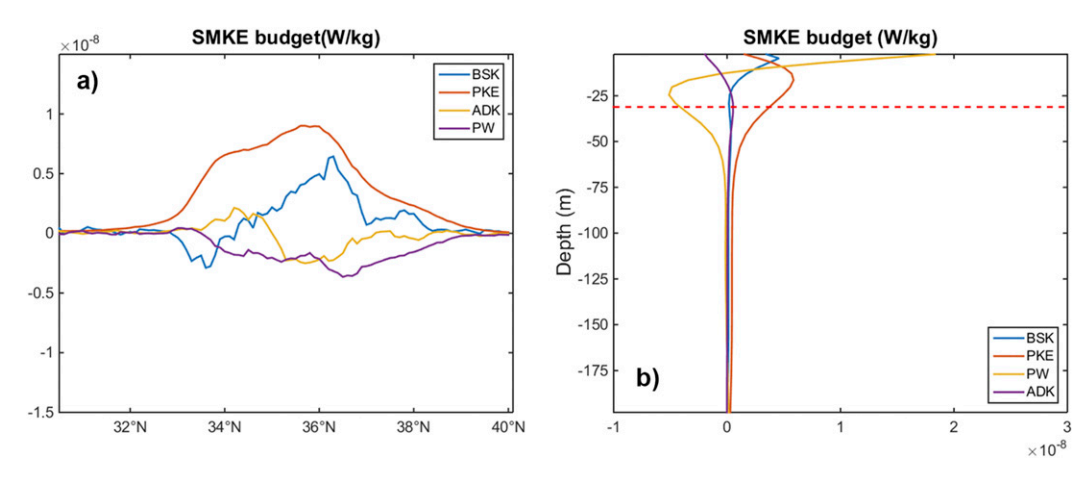


FIG. 8. (a) Vertically and zonally averaged, latitude-dependent plots and (b) horizontally averaged vertical profiles of SMKE production terms. The red dashed line denotes the averaged mixed layer depth of the whole research domain.

and intensified near the flow stream, consistent with the distribution of PKE. Thus, BSP—energy conversion from BPE to SMPE—serves as an important energy source for SMPE in the energy cycle (Fig. 2), probably arising from the horizontal concentration of density gradients by frontogenesis, submesoscale eddies, and winds. The BSP is also enhanced at the jet, which essentially results from the arrestment of cold filaments by horizontal shear instability (Gula et al. 2014). In a zonal-mean, vertical section plot (Fig. 10), the BSP mainly occurs in the middle of the mixed layer, consistent with the distribution of PKE (the gray dashed lines in Fig. 11). In contrast, the averaged ADP is small and seems to be insignificant for net SMPE production either in the latitude-dependent plot or in the horizontally averaged vertical profile (Fig. 11). Besides, ADP shows an opposite dependence on latitude than ADK (the orange line in Fig. 11a versus the yellow line in Fig. 8a); thus, the overall advection, a sum of ADP and ADK, has a slight contribution to the submesoscale energy. BndyPE is a nontrivial source of potential energy; however, unlike BndyKE, it is not sufficiently strong to affect the direction of energy flow from the BPE to the SMPE, i.e., both BSP and SBP agree that the potential energy transfer is toward smaller, faster scales

c. Energy pathways to the submesoscale

Figure 12 summarizes the upper-ocean energy cycle between the larger and slower background scales and the submesoscale. In the ROMS2 simulation (Fig. 12b), the submesoscale contains $0.69 \times 10^{-3} \,\mathrm{J\,kg^{-1}}$ of SMKE (averaged over the simulation period), followed by SMPE with an average amount of $0.51 \times 10^{-3} \,\mathrm{J\,kg^{-1}}$. The energy cycle displays two dominant, distinct routes of SMKE generation: BKE → SMKE through BSK and BPE \rightarrow SMPE \rightarrow SMKE through BSP and PKE. Statistically, the baroclinic energy conversion from SMPE to SMKE through PKE (3.42 in units of $10^{-9} \,\mathrm{W \, kg^{-1}}$) accounts for ~75% of the SMKE generation, dominating the possible direct wind-forced SMKE. Since none of the PW (0.61 \times $10^{-9} \, \mathrm{W \, kg^{-1}})$ and ADK $(0.02 \times 10^{-9} \, \mathrm{W \, kg^{-1}})$ is large enough to balance the SMKE, the remaining energy goes to parameterized or wind-induced dissipation $(3.91 \times 10^{-9} \,\mathrm{W\,kg^{-1}})$, estimated by assuming the SMKE is constant during the period $(\partial SMKE/\partial t = 0)$. The BSP provides about 60% of the SMPE

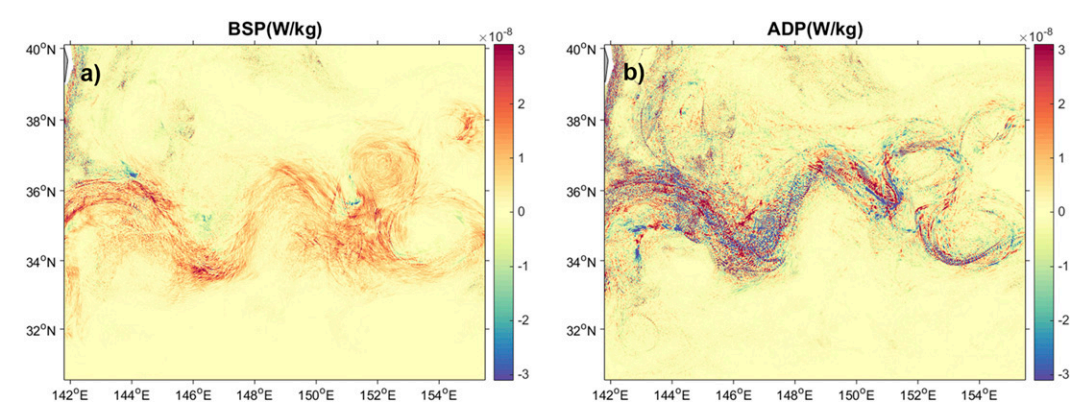


FIG. 9. Horizontal distribution of (a) BSP and (b) ADP averaged over the upper 50 m.

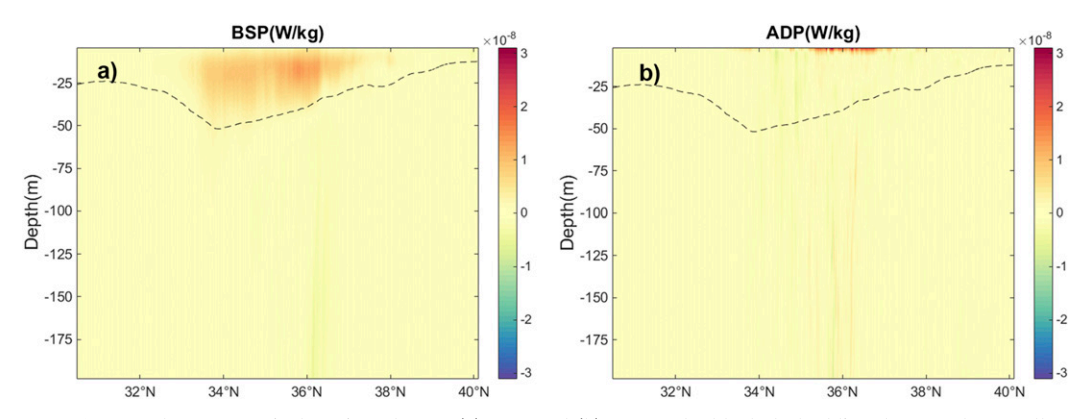


FIG. 10. Zonal-mean, vertical section plots of (a) BSP and (b) ADP. The black dashed line denotes the zonally averaged mixed layer depth.

that is subsequently transferred to SMKE through PKE, implying that a substantial portion of SMPE comes from the large-scale potential energy field (Fig. 12a). These results provide an important clue to the underlying submesoscale processes and their effects on the energy cycle (discussed in the following section). Note that the PKE is larger than the BSP (Fig. 12a), suggesting external submesoscale energy injection to SMPE, for example through wind forcing stimulating frontogenesis (Thomas et al. 2008). Note that the total wind stress effects on the submesoscale energy, SMKE + SMPE, are estimated to be minor compared to other effects. This implies that the wind work inputs some energy into SMPE but removes some of SMKE, consistent with the effects of mesoscale wind-eddy interaction in this region (Yang et al. 2019).

A rough estimate suggests that it takes approximately 1.76 days by the BSK and PKE together to fuel the SMKE reservoir as observed regardless of the other effects. This production time scale approximates the length of the life cycle of submesoscale features. The submesoscales are fast evolving and hardly retained if sources of energy were removed

[see Suzuki et al. (2016) for a decay time estimate for submesoscale fronts]. The submesoscale forward energy conversion rate in the mixed layer can reach a magnitude of $10^{-9} \,\mathrm{W\,kg^{-1}}$, comparable to the order of mesoscale effects estimated by Yang and Liang (2016) and submesoscale-induced turbulent dissipation rates found by D'Asaro et al. (2011) near the Kuroshio Extension. In contrast, mesoscale turbulence is normally characterized by an inverse KE cascade, whereas here a significant forward transfer from the background to the submesoscales is found.

Note that there exists a remarkable energy source for the KE $(4.90 \times 10^{-9} \, \text{W kg}^{-1})$ and a slight energy leakage for the PE $(0.21 \times 10^{-9} \, \text{W kg}^{-1})$ through the boundary in ROMS2. It is easiest to consider the significant BndyKE as a strong flux of energy from adjacent ocean domains that energizes the BKE field, which in turn energizes the submesoscale via BSK. However, if the convention for BndyKE is taken as arriving first in the SMKE, this interpretation implies a large positive SBK $(3.78 \times 10^{-9} \, \text{W kg}^{-1})$, indicating an inverse energy flow from the submesoscale to the background, while submesoscales

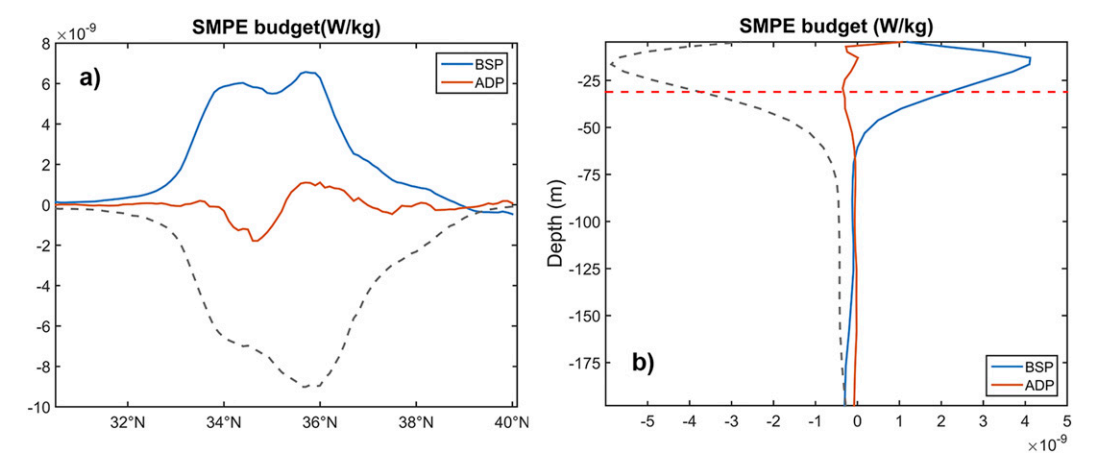


FIG. 11. (a) Vertically and zonally averaged, latitude-dependent plot and (b) horizontally averaged vertical profiles of SMPE production terms. The -PKE is also plotted in gray. The red dashed line denotes the averaged mixed layer depth of the whole research domain.

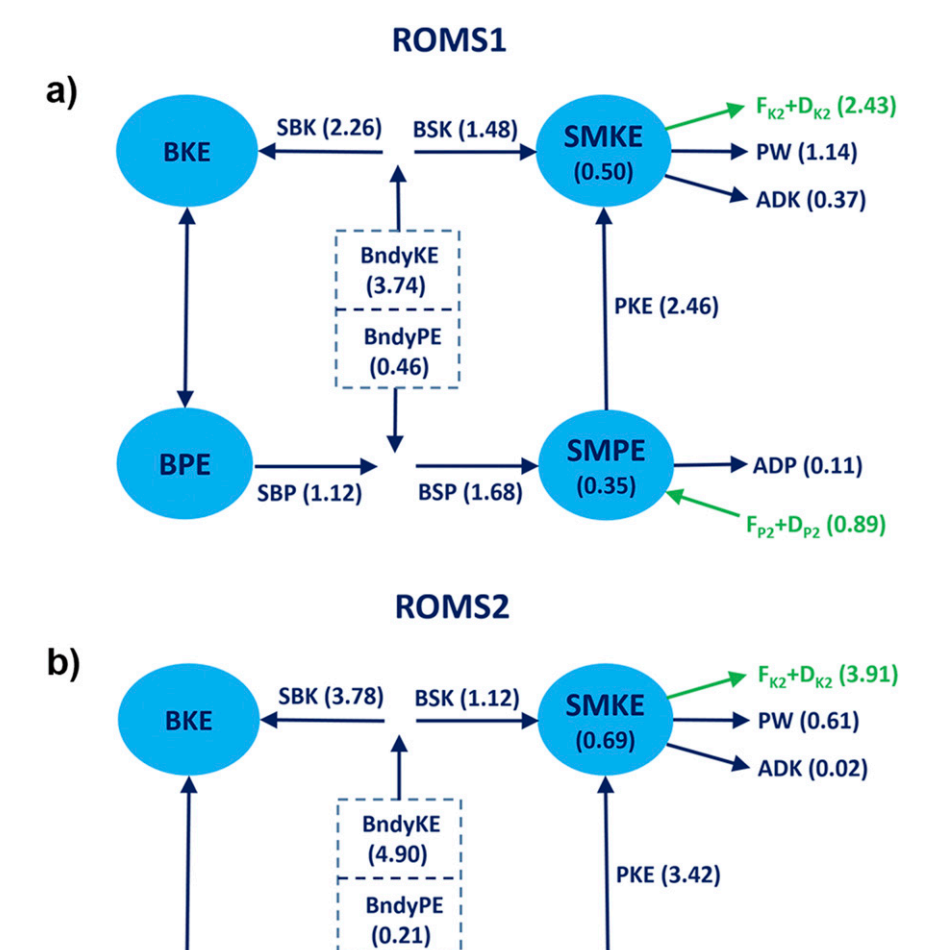


FIG. 12. Schematics of averaged energy conversion rates for ROMS1 and ROMS2 in units of $10^{-9}\,\mathrm{W\,kg^{-1}}$ and the energy reservoir in units of $10^{-3}\,\mathrm{J\,kg^{-1}}$. Compared to Fig. 2, the arrows illustrate the direction of energy transfers and energy leakage or source for boundary KE and PE. Note that the green arrows denote the combined effects of forcing and dissipation at the submesoscale when the SMKE and SMPE are assumed to be constant during the period $(\partial \mathrm{SMKE}/\partial t = 0)$ and $\partial \mathrm{SMPE}/\partial t = 0$.

BSP (2.06)

SMPE

(0.51)

are being strengthened by the KE field outside of the model domain. It is frankly confusing that the boundary source of KE is so large as to reverse the interpreted direction of transfer between the submesoscale and background scale based on a choice of convention. If the simulated region was bounded, there would be no interpretation required as the boundary terms would vanish. It is unclear to what extent an open domain plays a role in the interpretation of inverse and direct cascades in other studies (e.g., Schubert et al. 2020). It is reasonable that the upstream Kuroshio flow serves as an energy source for the generation of mesoscale and submesoscale eddies in the Kuroshio Extension. The boundary source of PE is small enough to cause less confusion, as at

BPE

SBP (2.27)

least SBP and BSP share the same direction from BPE to SMPE.

ADP (0.21)

 $F_{p2}+D_{p2}$ (1.57)

A comparison between the different resolution simulations ROMS2 and ROMS1 shows that most submesoscale energy production terms decrease in the lower-resolution simulation except for a slight increase in BSK. As mentioned above, BSK is an ensemble of several cancellatory effects, so one possible reason for an increase at coarser resolution is that the subcomponents of BSK fail to fully cancel each other out (the negative BSK in Fig. 6 is also supporting evidence). The sensitivity of these subcomponents to the horizontal resolution is further analyzed separately in the following section.

d. Sensitivity to horizontal resolution (ROMS1 vs ROMS2)

Figure 12 illustrates the different energy cycle quantities between ROMS2 (~0.5-km resolution) and ROMS1 (~1.5-km resolution). The increase of the reservoir of PKE from ROMS1 to ROMS2 is a matter of course as a deeper range of submesoscales are resolved by the ROMS2 simulation, but, surprisingly, the production of kinetic energy via BSK is reduced in the ROMS2 simulation. To obtain a more insightful understanding of the sensitivity of submesoscale energetics to horizontal resolution, we decompose BSK into six terms,

$$BSK_1 = -\overline{u'u'}\frac{\partial \overline{u}}{\partial x},\tag{16}$$

$$BSK_2 = -\overline{v'v'}\frac{\partial \overline{v}}{\partial y},\tag{17}$$

$$BSK_3 = -\overline{u'v'}\frac{\partial\overline{u}}{\partial y},\tag{18}$$

$$BSK_4 = -\overline{v'u'}\frac{\partial \overline{v}}{\partial x},\tag{19}$$

$$BSK_5 = -\overline{u'w'}\frac{\partial \overline{u}}{\partial z},\tag{20}$$

and

$$BSK_{6} = -\overline{v'w'}\frac{\partial \overline{v}}{\partial z},$$
(21)

where BSK₁ and BSK₂ are the contribution of diagonal horizontal Reynolds stress components, i.e., normal stresses (HRS), BSK₃ and BSK₄ are the torsional horizontal shear production (HSP), and BSK₅ and BSK₆ are the vertical shear production (VSP). Figure 13 compares the averaged energy terms (BSK₁, BSK₂, BSK₃, BSK₄, BSK₅, and BSK₆) between the ROMS1 and ROMS2 simulation. Among these terms, The BSK₂ (meridional normal Reynolds stress) and BSK4 (horizontal shear production from stresses associated with the meridional mean flow) turn out to be negative and tend to cancel the others. As such, the net BSK results from a competition between inverse (negative BSK) and forward (positive BSK) energy transfers. Indeed, in the ROMS2 simulation, each energy term is actually enhanced in magnitude while the overall net effect changes less (Fig. 13). The remarkable negative increase of BSK₂ and BSK₄ from ROMS1 to ROMS2 leads to the smaller BSK in the ROMS2 simulation.

In Fig. 14, the vertical profiles of the root-mean-square (RMS) values for each term are compared between the two simulations. The results show that the HRS and HSP are extremely active in the surface boundary layer, whereas the VSP peaks in the middle of the mixed layer, resembling the baroclinic production of submesoscale kinetic energy consistent with mixed layer vertical structures that extract and interact with multiple sources of energy (e.g., Haney et al. 2015). Ratios of RMS values between the ROMS1 and ROMS2 simulation help assess the sensitivity to the horizontal resolution (e.g., $R = \text{HSP}_{\text{MR}_{\text{RMS}}}/\text{HSP}_{\text{HR}_{\text{RMS}}}$, a smaller ratio means greater sensitivity). Figure 14d shows that VSP (the orange line) is most sensitive to the horizontal resolution, more so than HRS and

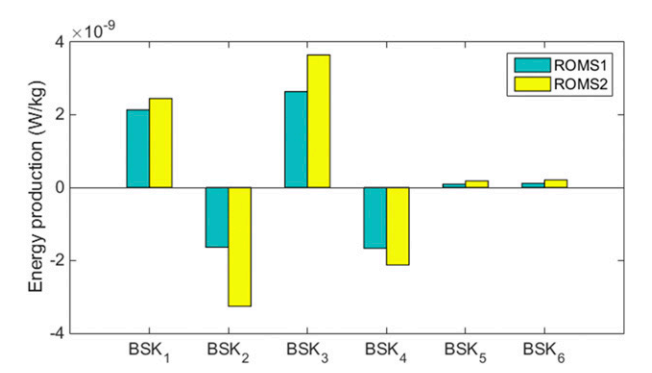


FIG. 13. Decomposed shear production (BSK) components averaged over the upper 50 m. The light blue bars are the ROMS1 simulation and yellow bars are the ROMS2 simulation. BSK₁ and BSK₂ denote energy production by normal horizontal Reynolds stresses (HRS); BSK₃ and BSK₄ denote horizontal shear production by torsional stresses (HSP); BSK₅ and BSK₆ denote vertical shear production (VSP).

HSP (purple and yellow lines) as a consequence of the enhanced submesoscale vertical velocity in ROMS2. At higher resolution, a nonhydrostatic model will become required as boundary layer turbulence becomes permitted when the horizontal grid rivals the boundary layer depth (Hamlington et al. 2014).

e. Scale-dependent energy budget

Submesoscale instabilities arise from a variety of mechanisms depending on the flow conditions: the barotropic shear production from the background flow dominates the production of SMKE in the tropical ocean study of Wang et al. (2018), whereas here baroclinic transfers from SMPE dominate. The mechanisms of this downscale transfer via BSK, consisting of the effects of normal strain and flow shear, deserve more detailed analysis. Figure 12 shows that the quantification of energy production remains sensitive to the horizontal resolution of numerical simulations, even at the high resolutions used here (\sim 0.5 and \sim 1.5 km). This is because some submesoscales, for example, slantwise symmetric instabilities, are only partly resolved, extract geostrophic kinetic energy, and give rise to downscale energy cascades (Taylor and Ferrari 2010; Thomas et al. 2013). The effects of SI are highly sensitive to resolution (Bachman and Taylor 2014).

BSK and PKE are the major SMKE production terms of the barotropic and baroclinic routes for forward energy transfers. In the barotropic modes, although a net downscale energy transfer by BSK is confirmed, the energy conversions in Fig. 12 highly depend on the cutoff scale defining the submesoscales. Here we revisit whether there is a sharp upper bound of the submesoscale (20 km) relevant to energy transfers via spectral SMKE generation:

$$\mathbf{E}_{\mathrm{BSK}}(k) = \Re \left[-\widehat{\mathbf{u}_{h}'} * \cdot (\widehat{\mathbf{u}' \cdot \nabla}) \overline{\mathbf{u}}_{h} \right], \tag{22}$$

$$E_{PKE}(k) = \Re\left[-\frac{g}{\rho_0} \widehat{w'} * \widehat{\rho'}\right], \tag{23}$$

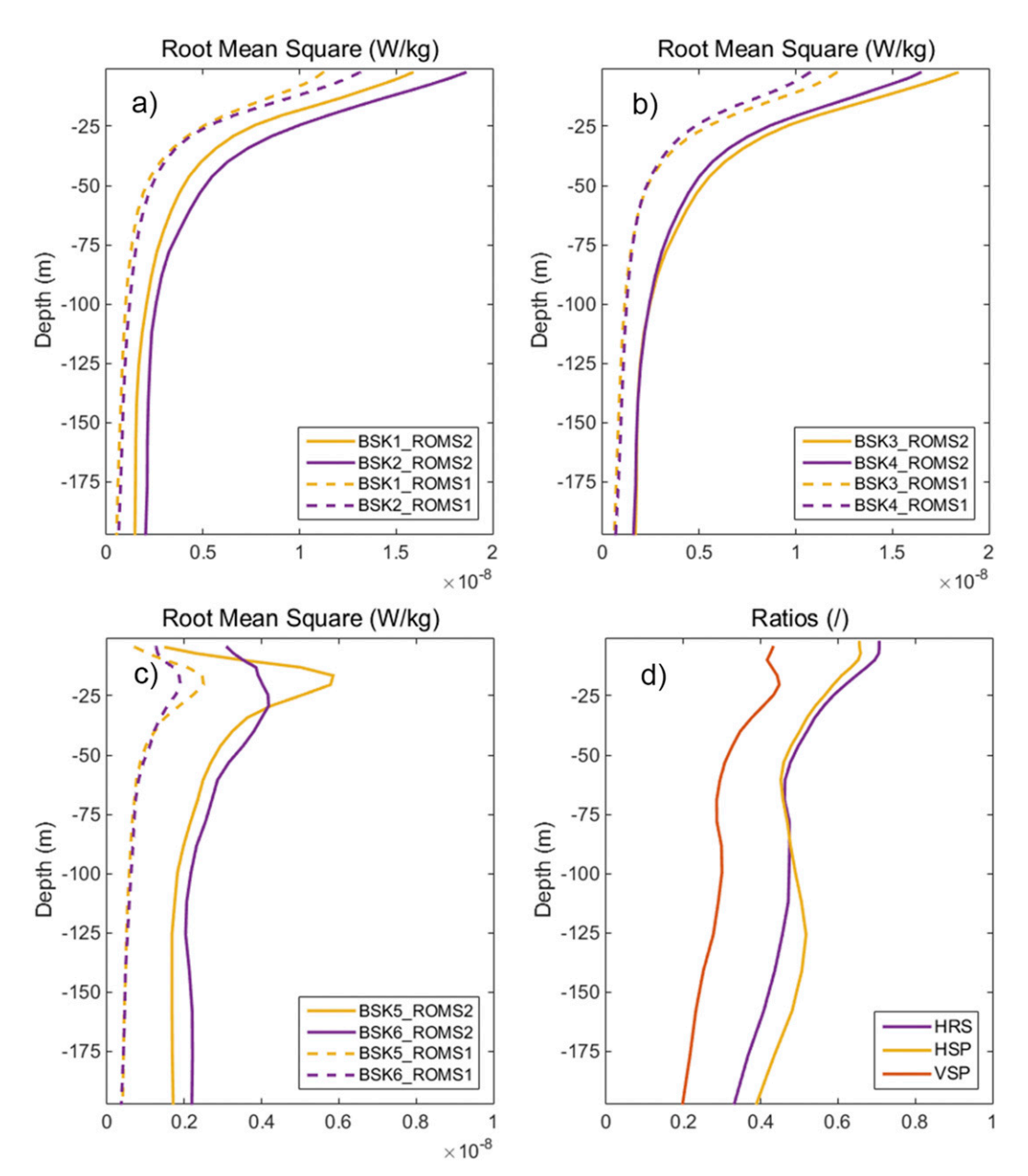


FIG. 14. Vertical profiles of root-mean-square values of (a) BSK1 and BSK2 [production by normal horizontal Reynolds stress (HRS)], (b) BSK3 and BSK4 (horizontal shear production by torsional stresses), and (c) BSK5 and BSK6 (vertical shear production) for the ROMS1 and ROMS2 simulation in the research domain. (d) Ratios between ROMS1 and ROMS2 simulation for HRS, HSP, and VSP.

$$\mathbf{E}_{\mathrm{PW}}(k) = \Re\left[-\frac{1}{\rho_0}\widehat{\mathbf{u}}^{\prime*} \cdot \widehat{\nabla p^{\prime}}\right],\tag{24}$$

$$\mathbf{E}_{\mathrm{ADK}}(k) = \Re\left[-\widehat{\mathbf{u}_{h}'} * \cdot (\mathbf{u}_{h}' \widehat{\cdot \nabla_{h}}) \mathbf{u}_{h}' - \widehat{\mathbf{u}_{h}'} * \cdot \widehat{\mathbf{w}'} \frac{\partial \mathbf{u}_{h}'}{\partial z}\right], \tag{25}$$

where ∇_h is the horizontal divergence operator, \Re is the symbol of the real part, and * is the complex conjugate. In this way, scale-dependent energy budgets can be estimated.

Figure 15 shows the spectral energy budget averaged over the upper 50 m. The PKE exhibits a dominant positive energy budget with a peak at a wavelength of ~ 15 km, where BSK reaches its negative maximum. With the decrease in the length scale, the BSK increases continuously and experiences a transition to positive (forward) values at ~ 10 km. The BSK has contrary impacts on the energy cascade above or below the transition scale. The negative peak of BSK is likely associated with the barotropized submesoscale energy from PKE that subsequently enters an inverse energy cascade (Callies et al. 2016;

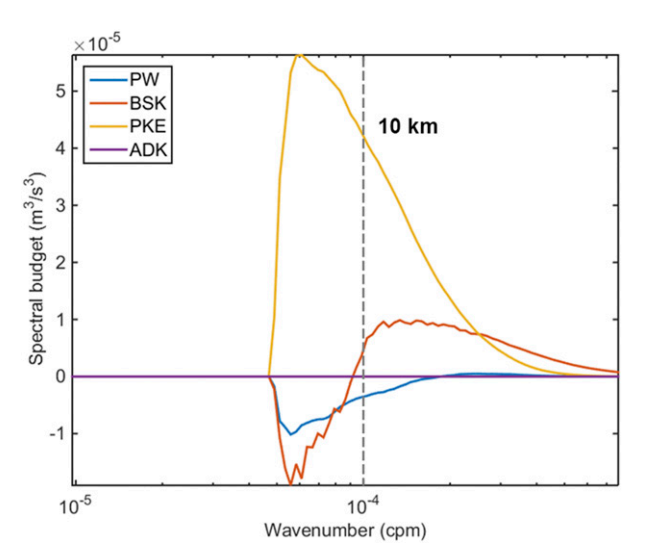


FIG. 15. Spectral pressure work (PW), background to submesoscale kinetic energy production (BSK), submesoscale potential to kinetic energy transfers (PKE), and advection of submesoscale kinetic energy (ADK) averaged over the upper 50 m. The dashed line indicates the wavelength of 10 km.

Schubert et al. 2020). This is attributed to the negative subcomponents of BSK shown in Fig. 13. A similar upscale energy transfer for submesoscale eddies in the upper ocean of the Agulhas Current system was recently reported (Schubert et al. 2020). Alternatively, it is defined as the submesoscale balanced KE (Torres et al. 2018) that tends to enter larger scales. Note that this is generated by the local submesoscale processes, distinct from the aforementioned SBK arising from the boundary effects. The positive peak of BSK occurs at wavelengths smaller than 10 km, consistent with the result of the divergence spectrum observed in Fig. 5. Hence, it is fair to infer that the divergence of flow could be a more typical feature for unbalanced submesoscale processes that can drive forward KE cascade at smaller submesoscales. Using the geostrophic unbalance to isolate the submesoscale range is dynamically meaningful in understanding that on these scales the submesoscale is quite unlike the mesoscale in Rossby number and horizontal divergence, so a downscale cascade of KE is one result. As such, the scale partition is critical for estimating the energy transfer between scales. As in this case, a decrease of the upper boundary will increase the BSK but reduce the PKE. A wavelength of 10 km seems to be critical if unbalanced submesoscale motions are of primary interest. As estimated in section 3 that about 10 times the grid spacing is required to well resolve a motion at a certain wavelength, the grid size for this case should be no larger than 1 km to evaluate the forward energy cascade correctly.

f. Scale dependence of transfers of KE and buoyancy production

A final consequence of the energy budget gives rise to the net injection or sink of kinetic and potential energy as functions of the length scale. The spectral KE flux can be defined as

$$\prod_{k} (k) = -\int_{k}^{k_{\text{max}}} E(k) \, dk, \tag{26}$$

where $E(k) = \Re[\hat{\mathbf{u}}_h^k \cdot (\hat{\mathbf{u}}_h \cdot \nabla) \mathbf{u}_h]$. Thus, the sign (negative or positive) of the flux implies the directions (inverse or forward) of the total KE cascade from larger to smaller scales (Scott and Wang 2005; Scott and Arbic 2007). Figure 16a shows the depth-dependent spectral KE flux in the upper ocean. The energy flux of KE tends to be upscale (negative) cascade at mesoscales above the transition scale (divided by the black line in Fig. 16a). The forward cascade (red shading in Fig. 16a) mainly occurs in the upper mixed layer, which is highly consistent with the vertical distribution of the BSK rather than the PKE (recall Fig. 7). The transition scale is ~ 25 km for the near-surface layer and quickly decreases to ~ 10 km in the middle of the mixed layer. In the main thermocline, the forward KE energy flux is dramatically reduced but still displays a slight forward energy cascade at scales less than 10 km.

Likewise, the spectral buoyancy flux can be defined as

$$\prod_{k=0}^{\infty} (k) = \int_{k}^{k_{\text{max}}} \Re(\hat{w}^* \hat{b}) dk.$$
 (27)

As shown in Fig. 16b, the buoyancy flux in the upper ocean is mostly positive, implying a continuous downscale cascade of the potential energy across the scales. The enhancement of the flux at $\sim 100 \, \mathrm{km}$ is likely associated with the generation of mesoscale eddies. In the submesoscale range, the buoyancy flux mainly exists within the mixed layer, consistent with the vertical distribution of PKE observed in Fig. 7b. The conversion of PE to KE serves as an important energy sink for the PE in the mesoscale energy cycle (Ferrari and Wunsch 2009) and is seemingly similar for the submesoscale found in this study. Note that the buoyancy flux in the mixed layer becomes much smaller at $\sim 10 \, \mathrm{km}$, indicative of weaker baroclinic effects at high wavenumbers in Fig. 16b (which agrees with the quick decrease of PKE at high wavenumbers in Fig. 15).

5. Summary

Submesoscale activities in the upper ocean act as a dynamical conduit between the mesoscale and the dissipation scale by providing substantial available potential energy and driving an effective forward kinetic and potential energy cascade. This work uses high-resolution simulations to investigate the submesoscale energetics in the upper ocean of the Kuroshio Extension region, with a focus on downscale energy transfers. It was found that both submesoscale kinetic and potential energy (SMKE and SMPE) play a significant role in converting energy to smaller scales through surface-trapped submesoscale modes. A large amount of submesoscale available potential energy is generated by stirring the heterogeneous surface buoyancy field, which is subsequently converted to submesoscale eddies through buoyancy production (as in Capet et al. 2016). Further analysis of the submesoscale energetics reveals the following:

 The frequency-wavenumber spectrum analysis identifies a broad-banded enhanced vertical vorticity and especially

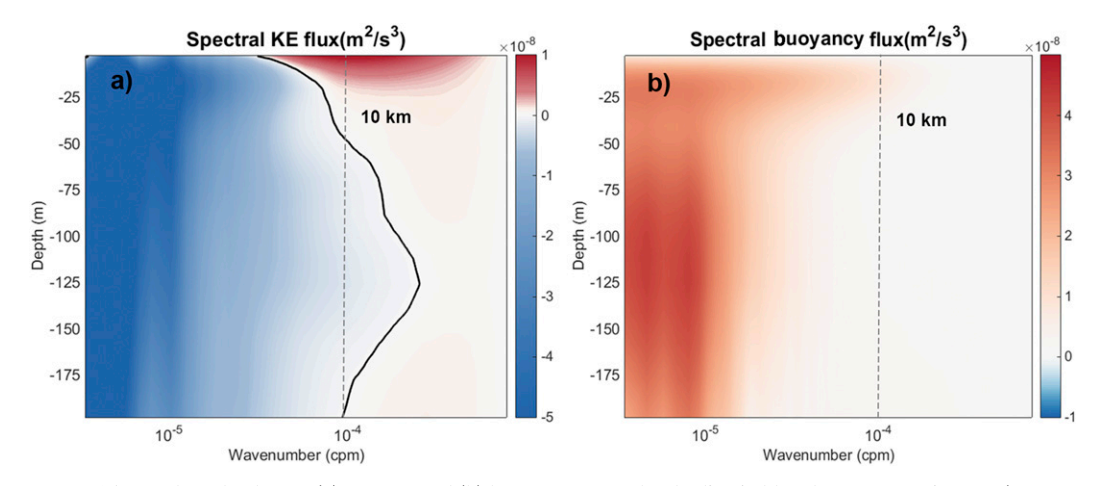


FIG. 16. Depth-scale plots of (a) KE flux and (b) buoyancy flux. The shading in blue denotes negative flux (energy transfer to larger scales) and the red shading means positive flux (energy transfer to smaller scales). The black solid line denotes the transition from negative to positive KE flux $[\Pi(k) = 0]$. The dashed lines indicate the wavelength of $10 \,\mathrm{km}$.

horizontal divergence in the high-frequency, high-wavenumber space, which are taken as the defining characteristics of geostrophically unbalanced submesoscale flows. This spectral characterization is distinct from that of narrow-banded inertial–gravity waves in frequency–wavenumber space.

- Submesoscale kinetic energy is generated mainly in the mixed layer by extracting energy from the mean flow. Both barotropic and baroclinic routes (BKE → SMKE and BPE → SMPE → SMKE) efficiently contribute to the generation of submesoscale phenomena.
- Shear production is particularly active in the near-surface layer and drives a forward energy cascade at the smaller submesoscales (i.e., unbalanced submesoscales); while baroclinic conversion of potential into kinetic energy dominates the middle mixed layer and generates submesoscale eddies.
 Some of the energy in these eddies subsequently enters an inverse KE cascade toward the larger submesoscales.
- Transfer of kinetic energy from the background to the submesoscales effectively contributes to a net forward (positive) KE transfer, although this contribution is an amalgam of normal Reynolds shear stress production (HRS), torsional Reynolds shear stress production (HSP), and vertical Reynolds shear stress production (VSP), which tend to cancel each other during eddy-mean interaction. All of these contributions are differently sensitive to horizontal resolution (~1.5 vs ~0.5 km). VSP is the most sensitive term, although it is the least significant component for the generation of SMKE at these resolutions.
- The KE and PE transfers from the outer domains provide a significant portion of energy budget—indeed, the KE flux from the outer domains is the largest term in the entire budget. Care is needed to understand this term together with the transfers between the background and submesoscale. In the approach chosen here, the boundary term energizes the background kinetic energy and then some of this energy is transferred downscale to the submesoscale. An alternative, equally legitimate framing (appendix) places the boundary flow of KE first in the submesoscale, which then cascades

upscale to the background flow. It is crucial in regional calculations to consider and understand that energy fluxes across scales can be contradictory in direction when such boundary terms are important as they are for KE here.

In this study, we mainly focused on the energy transfer routes by submesoscale processes in the upper ocean of the Kuroshio Extension region. A key finding is a method for identifying the scales dominated by submesoscale turbulence, which are distinct from the scales of submesoscale instabilities. Once identified, the next key point revealed is that the net forward energy transfers occur at scales that are small when compared to those of the mixed layer baroclinic instabilities. The complex energy cascade at submesoscales implies a great challenge in parameterizing the submesoscales for low-resolution numerical simulations. Seasonal variability of submesoscales is not discussed but it affects submesoscale processes by changing atmospheric forcing and background flow (Sasaki et al. 2014; Qiu et al. 2014; Rocha et al. 2016). Submesoscale processes should be enhanced as a response to the intensified atmospheric forcing in winter, although managing model and observation resolution consistently across seasons is an issue (Dong et al. 2020a). Energy pathways are similar across seasons, but their small changes can be revealing of the charging and discharging of different reservoirs (Dong et al. 2020b). Further studies of higher-resolution simulation and field observations are required to figure out the energetic details of submesoscale effects throughout the World Ocean, over the seasons, and over future climates.

Acknowledgments. The authors thank NASA (http://oceancolor.gsfc.nasa.gov) for the MODIS Aqua data and the QuikSCAT forcing (http://podaac.jpl.nasa.gov), NOAA ICOADS (http://icoads.noaa.gov), and SODA (https://www2.atmos.umd.edu/~ocean/) were also part of the forcing data. The data of U.S. KESS project (https://uskess.whoi.edu/overview/dataproducts/) were used to validate the velocity field in

the simulation. Source data for ROMS simulations are available at the scientific database of South China Sea Institute of Oceanology (www.scsio.csdb.cn). This study is supported by the National Natural Science Foundation of China (92058201, 51709092, 41776040, and 41949907). Haijin Cao is also partly supported by the National Key Research and Development Program of China grant (2017YFA0604104) and other projects (B200202139, LTO1907). Baylor Fox-Kemper is supported in part by NSF 1350795 and in part by NOAA NA19OAR4310366. Zhiyou Jing is partly supported by the Chinese Academy of Sciences (ZDBS-LY-DQC011, XDA15020901, and ISEE2018PY05).

APPENDIX

Energy Budget Equations

With the abovementioned energy definitions (Fig. 2), the energy budget equations with boundary terms for a fixed ocean domain are as follows. The BKE equation is expressed as

$$\frac{\partial}{\partial t}(BKE) = \underbrace{-\nabla \cdot [\overline{\mathbf{u}}(BKE)]}_{ADK_1} + BndyKE + \underbrace{(u'\mathbf{u}' \cdot \nabla \overline{u} + v'\mathbf{u}' \cdot \nabla \overline{v})}_{-BSK}$$

$$\underbrace{-\frac{1}{\rho_0}\nabla \cdot \overline{(\overline{\mathbf{u}}\overline{\rho})}}_{PW_1} - \underbrace{\frac{1}{\rho_0}g\overline{\rho}\overline{w}}_{PKE_1} + \overline{D}_{K1} + \overline{F}_{K1}, \quad (A1)$$

where the subscript 1 denotes the larger, slower scales. Then, the SMKE eqution becomes

$$\frac{\partial}{\partial t}(\text{SMKE}) = \underbrace{-\frac{1}{2}\nabla \cdot \left[\overline{\mathbf{u}(u'^2 + v'^2)}\right]}_{\text{ADK}_2} \underbrace{-\frac{1}{\rho_0}\nabla \cdot \left(\overline{\mathbf{u}'p'}\right)}_{\text{PW}_2} \underbrace{-\frac{1}{\rho_0}g\overline{\rho'w'}}_{\text{PKE}_2} \underbrace{-\frac{1}{\rho_0}g\overline{\rho'w'}}_{\text{PKE}_2} + \overline{D_{K2}} + \overline{F_{K2}}, \tag{A2}$$

where the subscript 2 denotes the submesoscale. Note that the energy leakage or source (BndyKE) works on the BKE budget in this formulation, and then BSK transfers energy from the BKE to the SMKE. However, SBK is the difference between BndyKE and BSK in Eq. (A1), so it is equally legitimate to consider the BndyKE as acting on the SMKE budget and then SBK is the transfer term from the submesoscale to the background. Thus, in Figs. 2 and 12, we illustrate the BndyKE term as arriving between the SMKE and BKE reservoirs. The expression of SBK is shown in Eq. (13).

Simarily, the energy equations for BPE and SMPE can be

$$\frac{\partial}{\partial t}(BPE) = \underbrace{-\nabla \cdot \overline{[\overline{\mathbf{u}}(BPE)]}}_{ADP_1} \underbrace{+\frac{1}{\rho_0} g\overline{\rho} \, \overline{w}}_{-PKE_1} + BndyPE$$

$$\underbrace{+\frac{g^2}{\rho_0^2 N^2} \overline{\rho' \mathbf{u}' \cdot \nabla \overline{\rho}}}_{-BSP} + \overline{D}_{P1} + \overline{F}_{P1}, \tag{A3}$$

$$\frac{\partial}{\partial t}(\text{SMPE}) = \underbrace{-\nabla \cdot \left[\mathbf{u} \left(\frac{g^2 \rho'^2}{2\rho_0^2 N^2}\right)\right]}_{\text{ADP}_2} \underbrace{-\frac{g^2}{\rho_0^2 N^2} \overline{\rho' \mathbf{u}' \cdot \nabla \overline{\rho}}}_{\text{BSP}} + \underbrace{\frac{1}{\rho_0} g \overline{\rho' w'}}_{-\text{PKE}_2} + \overline{D_{p_2}} + \overline{F_{p_2}}. \tag{A4}$$

The integrals of the boundary terms are

$$\int_{V} (BSK + SBK) dV = \int_{V} -\nabla_{i} (\overline{u_{j}u'_{j}u'_{i}}) dV = \oint_{S} -(\overline{u_{j}u'_{j}u'_{i}}) n_{i} dS,$$
(A5)

$$\int_{V} (BSP + SBP) dV = \int_{V} -\frac{g^{2}}{\rho_{0}^{2} N^{2}} \nabla_{i} \cdot (\overline{u'_{i} \rho' \overline{\rho}}) dV$$

$$= \oint_{S} -\frac{g^{2}}{\rho_{0}^{2} N^{2}} (\overline{u'_{i} \rho' \overline{\rho}}) n_{i} dS, \qquad (A6)$$

where the repeated indices indicate sums over i, j in all the directions (Einstein summation) and n_i is the outward normal vector component in the i direction. Note that the last form on the right always depends on a velocity oriented along the outward normal, thus global integrals bounded by basin boundaries will be zero. For a fixed ocean domain with open boundaries, the normal velocities are not zero [right-hand-sides of Eqs. (A5) and (A6)] and serve to exchange energy from (to) outer domains. The boundary terms can provide important energy source or leakage for the research domain as they do in this study.

REFERENCES

Aiki, H., and K. J. Richards, 2008: Energetics of the global ocean: The role of layer-thickness form drag. *J. Phys. Oceanogr.*, **38**, 1845–1869, https://doi.org/10.1175/2008JPO3820.1.

Arbic, B. K., M. Müller, J. G. Richman, J. F. Shriver, A. J. Morten, R. B. Scott, G. Sérazin, and T. Penduff, 2014: Geostrophic turbulence in the frequency-wavenumber domain: Eddy-driven low-frequency variability. *J. Phys. Oceanogr.*, 44, 2050–2069, https://doi.org/10.1175/JPO-D-13-054.1.

Bachman, S. D., and B. Fox-Kemper, 2013: Eddy parameterization challenge suite. I: Eady spindown. *Ocean Modell.*, 64, 12–28, https://doi.org/10.1016/j.ocemod.2012.12.003.

—, and J. R. Taylor, 2014: Modelling of partially-resolved oceanic symmetric instability. *Ocean Modell.*, 82, 15–27, https:// doi.org/10.1016/j.ocemod.2014.07.006.

—, B. Fox-Kemper, J. Taylor, and L. Thomas, 2017a: Parameterization of frontal symmetric instabilities. I: Theory for resolved fronts. *Ocean Modell.*, **109**, 72–95, https://doi.org/ 10.1016/j.ocemod.2016.12.003.

—, J. Taylor, K. Adams, and P. Hosegood, 2017b: Mesoscale and submesoscale effects on mixed layer depth in the Southern Ocean. J. Phys. Oceanogr., 47, 2173–2188, https://doi.org/10.1175/ JPO-D-17-0034.1.

Boccaletti, G., R. Ferrari, and B. Fox-Kemper, 2007: Mixed layer instabilities and restratification. *J. Phys. Oceanogr.*, **37**, 2228–2250, https://doi.org/10.1175/JPO3101.1.

Brannigan, L., D. Marshall, A. N. Garabato, A. J. G. Nurser, and J. Kaiser, 2017: Submesoscale instabilities in mesoscale eddies. *J. Phys. Oceanogr.*, 47, 3061–3085, https://doi.org/10.1175/ JPO-D-16-0178.1.

Buckingham, C., and Coauthors, 2016: Seasonality of submesoscale flows in the ocean surface boundary layer. *Geophys. Res. Lett.*, **43**, 2118–2126, https://doi.org/10.1002/2016GL068009.

- —, Z. Khaleel, A. Lazar, A. Martin, J. Allen, A. N. Garabato, A. Thompson, and C. Vic, 2017: Testing Munk's hypothesis for submesoscale eddy generation using observations in the North Atlantic. J. Geophys. Res. Oceans, 122, 6725–6745, https:// doi.org/10.1002/2017JC012910.
- Callies, J., R. Ferrari, J. M. Klymak, and J. Gula, 2015: Seasonality in submesoscale turbulence. *Nat. Commun.*, 6, 6862, https:// doi.org/10.1038/ncomms7862.
- —, G. Flierl, R. Ferrari, and B. Fox-Kemper, 2016: The role of mixed-layer instabilities in submesoscale turbulence. *J. Fluid Mech.*, 788, 5–41, https://doi.org/10.1017/jfm.2015.700.
- Cao, H., Z. Jing, B. Fox-kemper, T. Yan, and Y. Qi, 2019: Scale transition from geostrophic motions to internal waves in the northern South China Sea. J. Geophys. Res. Oceans, 124, 9364–9383, https://doi.org/10.1029/2019JC015575.
- Capet, X., J. McWilliams, M. Molemaker, and A. Shchepetkin, 2008a: Mesoscale to submesoscale transition in the California Current System. Part I: Flow structure, eddy flux, and observational tests. J. Phys. Oceanogr., 38, 29–43, https://doi.org/ 10.1175/2007JPO3671.1.
- —, —, and —, 2008b: Mesoscale to submesoscale transition in the California Current System. Part III: Energy balance and flux. *J. Phys. Oceanogr.*, **38**, 2256–2269, https://doi.org/10.1175/2008JPO3810.1.
- —, G. Roullet, P. Klein, and G. Maze, 2016: Intensification of upper-ocean submesoscale turbulence through Charney baroclinic instability. *J. Phys. Oceanogr.*, 46, 3365–3384, https:// doi.org/10.1175/JPO-D-16-0050.1.
- Capuano, T. A., S. Speich X. Carton, and B. Blanke, 2018: Mesoscale and submesoscale processes in the southeast Atlantic and their impact on the regional thermohaline structure. *J. Geophys. Res. Oceans*, 123, 1937–1961, https://doi.org/ 10.1002/2017JC013396.
- Carton, J., and B. Giese, 2008: A reanalysis of ocean climate using Simple Ocean Data Assimilation (SODA). Mon. Wea. Rev., 136, 2999–3017, https://doi.org/10.1175/2007MWR1978.1.
- Charney, J. G., 1971: Geostrophic turbulence. *J. Atmos. Sci.*, **28**, 1087–1095, https://doi.org/10.1175/1520-0469(1971)028<1087: GT>2.0.CO;2.
- Chen, R., G. R. Flierl, and C. Wunsch, 2014: A description of local and nonlocal eddy-mean flow interaction in a global eddypermitting state estimate. J. Phys. Oceanogr., 44, 2336–2352, https://doi.org/10.1175/JPO-D-14-0009.1.
- Cronin, M., and D. Watts, 1996: Eddy-mean flow interaction in the Gulf Stream at 68°W. Part I: Eddy energetics. *J. Phys. Oceanogr.*, **26**, 2107–2131, https://doi.org/10.1175/1520-0485(1996)026<2107:EFIITG>2.0.CO;2.
- D'Asaro, E. A., C. Lee, L. Rainville, R. Harcourt, and L. Thomas, 2011: Enhanced turbulence and energy dissipation at ocean fronts. *Science*, 332, 318–322, https://doi.org/10.1126/science.1201515.
- —, and Coauthors, 2018: Ocean convergence and the dispersion of flotsam. *Proc. Natl. Acad. Sci. USA*, **115**, 1162–1167, https:// doi.org/10.1073/pnas.1718453115.
- —, and Coauthors, 2020: Advances in observing and understanding small-scale open ocean circulation during the Gulf of Mexico research initiative era. Front. Mar. Sci., 7, 349, https:// doi.org/10.3389/fmars.2020.00349.
- de Boyer Montégut, C., G. Madec, A. Fischer, A. Lazar, and D. Iudicone, 2004: Mixed layer depth over the global ocean: An examination of profile data and a profile-based climatology. J. Geophys. Res., 109, C12003, https://doi.org/10.1029/2004JC002378.
- Dong, J., B. Fox-Kemper, H. Zhang, and C. Dong, 2020a: The size of submesoscale baroclinic instability globally. *J. Phys.*

- Oceanogr., **50**, 2649–2667, https://doi.org/10.1175/JPO-D-20-0043.1.
- —, —, and —, 2020b: The seasonality of submesoscale energy production, content, and cascade. *Geophys. Res. Lett.*, **47**, e2020GL087388, https://doi.org/10.1029/2020GL087388.
- du Plessis, M., S. Swart, I. J. Ansorge, A. Mahadevan, and A. F. Thompson, 2019: Southern ocean seasonal restratification delayed by submesoscale wind-front interactions. *J. Phys. Oceanogr.*, 49, 1035–1053, https://doi.org/10.1175/JPO-D-18-0136.1.
- Ferrari, R., and C. Wunsch, 2009: Ocean circulation kinetic energy: Reservoirs, sources, and sinks. *Annu. Rev. Fluid Mech.*, **41**, 253–282, https://doi.org/10.1146/annurev.fluid.40.111406.
- Fox-Kemper, B., R. Ferrari, and R. Hallberg, 2008: Parameterization of mixed layer eddies. Part I: Theory and diagnosis. J. Phys. Oceanogr., 38, 1145–1165, https://doi.org/10.1175/2007JPO3792.1.
- Gentemann, C. L., and Coauthors, 2020: Saildrone: Adaptively sampling the marine environment. *Bull. Amer. Meteor. Soc.*, 101, E744–E762, https://doi.org/10.1175/BAMS-D-19-0015.1.
- Gill, A., 1982: Atmosphere-Ocean Dynamics. Academic Press, 662 pp.
- Grooms, I., L. Nadeau, and K. Smith, 2013: Mesoscale eddy energy locality in an idealized ocean model. J. Phys. Oceanogr., 43, 1911–1923, https://doi.org/10.1175/JPO-D-13-036.1.
- Gula, J., M. Molemaker, and J. McWilliams, 2014: Submesoscale cold filaments in the Gulf Stream. J. Phys. Oceanogr., 44, 2617–2643, https://doi.org/10.1175/JPO-D-14-0029.1.
- Hamlington, P. E., L. P. Van Roekel, B. Fox-Kemper, K. Julien, and G. P. Chini, 2014: Langmuir-submesoscale interactions: Descriptive analysis of multiscale frontal spindown simulations. J. Phys. Oceanogr., 44, 2249–2272, https://doi.org/10.1175/JPO-D-13-0139.1.
- Haney, S., B. Fox-Kemper, K. Julien, and A. Webb, 2015: Symmetric and geostrophic instabilities in the wave-forced ocean mixed layer. *J. Phys. Oceanogr.*, 45, 3033–3056, https:// doi.org/10.1175/JPO-D-15-0044.1.
- Holopainen, E. O., 1978: A diagnostic study on the kinetic energy balance of the long-term mean flow and the associated transient fluctuation in the atmosphere. *Geophysica*, 15, 125–145.
- Hoskins, B. J., 1974: The role of potential vorticity in symmetric stability and instability. *Quart. J. Roy. Meteor. Soc.*, **100**, 480–482, https://doi.org/10.1002/qj.49710042520.
- Huang, R. X., 1999: Mixing and energetics of the oceanic thermohaline circulation. J. Phys. Oceanogr., 29, 727–746, https://doi.org/10.1175/1520-0485(1999)029<0727: MAEOTO>2.0.CO:2.
- Jamet, Q., A. Ajayi, J. L. Sommer, T. Penduff, A. Hogg, and W. K. Dewar, 2020: On energy cascades in general flows: A Lagrangian application. *J. Adv. Model. Earth Syst.*, 12, e2020MS002090, https://doi.org/10.1029/2020MS002090.
- Jiao, Y., and W. K. Dewar, 2015: The energetics of centrifugal instability. J. Phys. Oceanogr., 45, 1554–1573, https://doi.org/ 10.1175/JPO-D-14-0064.1.
- Jing, Z., Y. Qi, B. Fox-Kemper, Y. Du, and S. Lian, 2016: Seasonal thermal fronts and their associations with monsoon forcing on the continental shelf of northern South China Sea: Satellite measurements and three repeated field surveys in winter, spring and summer. J. Geophys. Res. Oceans, 121, 1914–1930, https://doi.org/10.1002/2015JC011222.
- ——, B. Fox-Kemper, H. Cao, R. Zheng, and Y. Du, 2021: Submesoscale fronts and their dynamical processes associated with symmetric instability in the northwest Pacific subtropical Ocean. J. Phys. Oceanogr., 51, 83–100, https://doi.org/10.1175/ JPO-D-20-0076.1.

- Kang, D., and O. B. Fringer, 2010: On the calculation of available potential energy in internal wave fields. J. Phys. Oceanogr., 40, 2539–2545, https://doi.org/10.1175/2010JPO4497.1.
- —, and E. N. Curchitser, 2015: Energetics of eddy-mean flow interactions in the Gulf Stream region. *J. Phys. Oceanogr.*, 45, 1103–1120, https://doi.org/10.1175/JPO-D-14-0200.1.
- Klein, P., B. L. Hua, G. Lapeyre X. Capet, S. Le Gentil, and H. Sasaki, 2008: Upper ocean turbulence from high-resolution 3D simulations. *J. Phys. Oceanogr.*, 38, 1748–1763, https://doi.org/10.1175/2007JPO3773.1.
- Klocker, A., D. Marshall, S. Keating, and P. Read, 2016: A regime diagram for ocean geostrophic turbulence. *Quart. J. Roy. Meteor. Soc.*, **142**, 2411–2417, https://doi.org/10.1002/qj.2833.
- Kraichnan, R. H., 1967: Inertial ranges in two-dimensional turbulence. *Phys. Fluids*, **10**, 1417–1423, https://doi.org/10.1063/1.1762301.
- Large, W., J. McWilliams, and S. Doney, 1994: Oceanic vertical mixing: A review and a model with a nonlocal boundary layer parameterization. *Rev. Geophys.*, 32, 363–403, https://doi.org/ 10.1029/94RG01872.
- Lemarié, F., J. Kurian, A. F. Shchepetkin, M. J. Molemaker, F. Colas, and J. C. McWilliams, 2012: Are there inescapable issues prohibiting the use of terrain-following coordinates in climate models? *Ocean Modell.*, 42, 57–79, https://doi.org/ 10.1016/j.ocemod.2011.11.007.
- Lévy, M., P. Klein, and A. Tréguier, 2001: Impact of sub-mesoscale physics on production and subduction of phytoplankton in an oligotrophic regime. J. Mar. Res., 59, 535–565, https://doi.org/ 10.1357/002224001762842181.
- —, D. Iovino, L. Resplandy, P. Klein, G. Madec, A. Tréguier, S. Masson, and K. Takahashi, 2012: Large-scale impacts of submesoscale dynamics on phytoplankton: Local and remote effects. *Ocean Modell.*, 43-44, 77–93, https://doi.org/10.1016/ j.ocemod.2011.12.003.
- Lorenz, E. N., 1955: Available potential energy and the maintenance of the general circulation. *Tellus*, 7, 157–167, https:// doi.org/10.3402/tellusa.v7i2.8796.
- Mahadevan, A., and A. Tandon, 2006: An analysis of mechanisms for submesoscale vertical motion at ocean fronts. *Ocean Modell.*, 14, 241–256, https://doi.org/10.1016/j.ocemod.2006.05.006.
- McWilliams, J., 2016: Submesoscale currents in the ocean. *Proc. Roy. Soc.*, 472A, 20160117, https://doi.org/10.1098/rspa.2016.0117.
- Molemaker, M., J. McWilliams, and X. Capet, 2010: Balanced and unbalanced routes to dissipation in an equilibrated Eady flow. J. Fluid Mech., 654, 35–63, https://doi.org/10.1017/ S0022112009993272.
- Munk, W., L. Armi, K. Fischer, and F. Zachariasen, 2000: Spirals on the sea. *Proc. Roy. Soc.*, **456A**, 1217–1280, https://doi.org/ 10.1098/rspa.2000.0560.
- Nakamura, H., and A. Kazmin, 2003: Decadal changes in the North Pacific oceanic frontal zones as revealed in ship and satellite observations. J. Geophys. Res., 108, 3078, https://doi.org/ 10.1029/1999JC000085.
- Pearson, B., and B. Fox-Kemper, 2018: Log-normal turbulence dissipation in global ocean models. *Phys. Rev. Lett.*, **120**, 094501, https://doi.org/10.1103/PhysRevLett.120.094501.
- —, —, S. D. Bachman, and F. O. Bryan, 2017: Evaluation of scale-aware subgrid mesoscale eddy models in a global eddy-rich model. *Ocean Modell.*, 115, 42–58, https://doi.org/ 10.1016/j.ocemod.2017.05.007.
- Pearson, J., B. Fox-Kemper, R. Barkan, J. Choi, A. Bracco, and J. C. McWilliams, 2019: Impacts of convergence on structure functions from surface drifters in the Gulf of Mexico. J. Phys.

- Oceanogr., 49, 675–690, https://doi.org/10.1175/JPO-D-18-0029.1.
- —, and Coauthors, 2020: Biases in structure functions from observations of submesoscale flows. *J. Geophys. Res. Oceans*, 125, e2019JC015769, https://doi.org/10.1029/2019JC015769.
- Plumb, R. A., 1983: A new look at the energy cycle. J. Atmos. Sci., 40, 1669–1688, https://doi.org/10.1175/1520-0469(1983)040<1669: ANLATE>2.0.CO:2.
- Qiu, B., 2000: Interannual variability of the Kuroshio Extension system and its impact on the wintertime SST field. *J. Phys. Oceanogr.*, **30**, 1486–1502, https://doi.org/10.1175/1520-0485(2000) 030<1486:IVOTKE>2.0.CO;2.
- —, and S. Chen, 2005: Variability of the Kuroshio Extension jet, recirculation gyre, and mesoscale eddies on decadal time scales. *J. Phys. Oceanogr.*, 35, 2090–2103, https://doi.org/10.1175/JPO2807.1.
- —, K. Kelly, and T. Joyce, 1991: Mean flow and variability in the Kuroshio Extension from Geosat altimetry data. *J. Geophys. Res.*, **96**, 18491–18507, https://doi.org/10.1029/91JC01834.
- —, S. Chen, P. Klein, H. Sasaki, and Y. Sasai, 2014: Seasonal mesoscale and submesoscale eddy variability along the North Pacific subtropical countercurrent. *J. Phys. Oceanogr.*, 44, 3079–3098, https://doi.org/10.1175/JPO-D-14-0071.1.
- Rocha, C. B., S. Gille, T. Chereskin, and D. Menemenlis, 2016: Seasonality of submesoscale dynamics in the Kuroshio Extension. *Geophys. Res. Lett.*, 43, 11304–11311, https://doi.org/10.1002/2016GL071349.
- Rosso, I., A. Hogg, P. Strutton, A. Kiss, R. Matear, A. Klocker, and E. van Sebille, 2014: Vertical transport in the ocean due to submesoscale structures: Impacts in the Kerguelen region. *Ocean Modell.*, 80, 10–23, https://doi.org/10.1016/j.ocemod.2014.05.001.
- Saenz, J. A., R. Tailleux, E. D. Butler, G. O. Hughes, and K. I. Oliver, 2015: Estimating Lorenz's reference state in an ocean with a nonlinear equation of state for seawater. *J. Phys. Oceanogr.*, 45, 1242–1257, https://doi.org/10.1175/JPO-D-14-0105.1.
- Sasaki, H., P. Klein, B. Qiu, and Y. Sasai, 2014: Impact of oceanic-scale interactions on the seasonal modulation of ocean dynamics by the atmosphere. *Nat. Commun.*, 5, 5636, https://doi.org/10.1038/ncomms6636.
- Schubert, R., J. Gula, R. J. Greatbatch, B. Baschek, and A. Biastoch, 2020: The submesoscale kinetic energy cascade: Mesoscale absorption of submesoscale mixed layer eddies and frontal downscale fluxes. J. Phys. Oceanogr., 50, 2573–2589, https:// doi.org/10.1175/JPO-D-19-0311.1.
- Scott, R. B., and F. Wang, 2005: Direct evidence of an oceanic inverse kinetic energy cascade from satellite altimetry. J. Phys. Oceanogr., 35, 1650–1666, https://doi.org/10.1175/JPO2771.1.
- ——, and B. K. Arbic, 2007: Spectral energy fluxes in geostrophic turbulence: Implications for ocean energetics. *J. Phys. Oceanogr.*, 37, 673–688, https://doi.org/10.1175/JPO3027.1.
- Shchepetkin, A. F., and J. C. McWilliams, 2005: The Regional Oceanic Modeling System (ROMS): A split-explicit, free-surface, topography-following-coordinate oceanic model. *Ocean Modell.*, 9, 347–404, https://doi.org/10.1016/j.ocemod.2004.08.002.
- —, and J. McWilliams, 2009: Correction and commentary for "Ocean forecasting in terrain-following coordinates: Formulation and skill assessment of the regional ocean modeling system." J. Comput. Phys., 228, 8985–9000, https://doi.org/10.1016/ j.jcp.2009.09.002.
- Shcherbina, A., E. D'Asaro, C. Lee, J. Klymak, M. Molemaker, and J. McWilliams, 2013: Statistics of vertical vorticity, divergence, and strain in a developed submesoscale turbulence field. *Geophys. Res. Lett.*, 40, 4706–4711, https://doi.org/10.1002/grl.50919.

- Suzuki, N., B. Fox-Kemper, P. E. Hamlington, and L. P. Van Roekel, 2016: Surface waves affect frontogenesis. *J. Geophys. Res. Oceans*, 121, 3597–3624, https://doi.org/10.1002/2015JC011563.
- Tai, C., and W. White, 1990: Eddy variability in the Kuroshio Extension as revealed by Geosat altimetry: Energy propagation away from the jet, Reynolds stress, and seasonal cycle. *J. Phys. Oceanogr.*, 20, 1761–1777, https://doi.org/10.1175/1520-0485(1990)020<1761:EVITKE>2.0.CO;2.
- Taylor, J. R., and R. Ferrari, 2010: Buoyancy and wind-driven convection at mixed layer density fronts. J. Phys. Oceanogr., 40, 1222–1242, https://doi.org/10.1175/2010JPO4365.1.
- Thomas, L., A. Tandon, and A. Mahadevan, 2008: Submesoscale processes and dynamics. *Ocean Modeling in an Eddying Regime, Geophys. Monogr.*, Vol. 177, Amer. Geophys. Union, 17–38.
- —, J. Taylor, R. Ferrari, and T. Joyce, 2013: Symmetric instability in the Gulf Stream. *Deep-Sea Res. II*, 91, 96–110, https://doi.org/10.1016/j.dsr2.2013.02.025.
- Thompson, A., A. Lazar, C. Buckingham, A. Naveira Garabato, G. Damerell, and K. Heywood, 2016: Open-ocean submesoscale motions: A full seasonal cycle of mixed layer instabilities from gliders. J. Phys. Oceanogr., 46, 1285–1307, https://doi.org/10.1175/JPO-D-15-0170.1.
- Torres, H., P. Klein, D. Menemenlis, B. Qiu, Z. Su, J. Wang, S. Chen, and L. Fu, 2018: Partitioning ocean motions into balanced motions and internal gravity waves: A modeling study in anticipation of future space missions. *J. Geophys. Res. Oceans*, 123, 8084–8105, https://doi.org/10.1029/2018JC014438.
- Tulloch, R., J. Marshall, and C. Hill, 2011: Scales, growth rates, and spectral fluxes of baroclinic instability in the ocean. *J. Phys. Oceanogr.*, **41**, 1057–1076, https://doi.org/10.1175/2011JPO4404.1.
- Villas Boas, A. B., and Coauthors, 2019: Integrated observations and modeling of winds, currents, and waves: Requirements

- and challenges for the next decade. Front. Mar. Sci., 6, 425, https://doi.org/10.3389/fmars.2019.00425.
- Wang, S., Z. Jing, H. Liu, and L. Wu, 2018: Spatial and seasonal variations of submesoscale eddies in the eastern tropical Pacific Ocean. J. Phys. Oceanogr., 48, 101–116, https://doi.org/ 10.1175/JPO-D-17-0070.1.
- Waterman, S., N. Hogg, and S. Jayne, 2011: Eddy-mean flow interaction in the Kuroshio Extension region. J. Phys. Oceanogr., 41, 1182–1208, https://doi.org/10.1175/2010JPO4564.1.
- Woodruff, S., and Coauthors, 2011: ICOADS release 2.5: Extensions and enhancements to the surface marine meteorological archive. *Int. J. Climatol.*, 31, 951–967, https://doi.org/10.1002/joc.2103.
- Yan, X., D. Kang, E. N. Curchitser, and C. Pang, 2019: Energetics of eddy-mean flow interactions along the western boundary currents in the North Pacific. J. Phys. Oceanogr., 49, 789–810, https://doi.org/10.1175/JPO-D-18-0201.1.
- Yang, H., P. Chang, B. Qiu, Q. Zhang, L. Wu, Z. Chen, and H. Wang, 2019: Mesoscale air–sea interaction and its role in eddy energy dissipation in the Kuroshio Extension. *J. Climate*, 32, 8659–8676, https://doi.org/10.1175/JCLI-D-19-0155.1.
- Yang, Y., and X. Liang, 2016: The instabilities and multiscale energetics underlying the mean–interannual–eddy interactions in the Kuroshio Extension region. *J. Phys. Oceanogr.*, 46, 1477–1494, https://doi.org/10.1175/JPO-D-15-0226.1.
- Zhang, Z., J. Tian, B. Qiu, W. Zhao, P. Chang, D. Wu, and X. Wan, 2016: Observed 3D structure, generation, and dissipation of oceanic mesoscale eddies in the South China Sea. Sci. Rep., 6, 24349, https://doi.org/10.1038/srep24349.
- ——, X. Zhang, B. Qiu, W. Zhao, C. Zhou, X. Huang, and J. Tian, 2021: Submesoscale currents in the subtropical upper ocean observed by long-term high-resolution mooring arrays. J. Phys. Oceanogr., 51, 187–206, https://doi.org/10.1175/JPO-D-20-0100.1.